REPORT NO. FAA-RD-74-29

# THE MEASUREMENT OF ATMOSPHERIC VISIBILITY WITH LIDAR: TSC FIELD TEST RESULTS

J.R. Lifsitz


MARCH 1974
FINAL REPORT



Prepared for
DEPARTMENT OF TRANSPORTATION
FEDERAL AVIATION ADMINISTRATION
Systems Research and Development Service
Washington DC 20591

**Technical Report Documentation Page**

| 1. Report No. | 2. Government Accession No. | 3. Recipient's Catalog No. |
|---|---|---|
| FAA-RD-74-29 | | |

| 4. Title and Subtitle | 5. Report Date |
|---|---|
| THE MEASUREMENT OF ATMOSPHERIC VISIBILITY WITH LIDAR: TSC FIELD TEST RESULTS | March 1974 |
| | 6. Performing Organization Code |
| 7. Author(s) J. R. Lifsitz | 8. Performing Organization Report No. DOT-TSC-FAA-73-27 |
| 9. Performing Organization Name and Address Department of Transportation Transportation Systems Center Kendall Square Cambridge MA 02142 | 10. Work Unit No. (TRAIS) FA415/R4138 |
| | 11. Contract or Grant No. |
| 12. Sponsoring Agency Name and Address Department of Transportation Federal Aviation Administration Systems Research and Development Service Washington DC 20591 | 13. Type of Report and Period Covered Final Report June 1972 - June 1973 |
| | 14. Sponsoring Agency Code |

15. Supplementary Notes

16. Abstract

This report represents a technical feasibility study of the use of lidar for determining the atmospheric extinction coefficient ($\sigma$) in low visibility. Measurements were made with three laser sources: a Q-switched ruby laser, a GaAlAs diode laser array, and a modulated cw helium-neon laser. The work, sponsored by the FAA, is part of a program aimed at measuring and reporting slant visibility.

Results of lidar measurements made both in natural coastal fog and in artificial fog are analyzed. Extinction coefficients ($.01 < \sigma < .07 m^{-1}$) are obtained with the pulsed systems, using both the "slope" and "ratio" methods to analyze the backscatter signature. Corrections for finite laser pulse width are included in the data reduction. The analysis does not treat the effects of multiple scattering. In most cases the pulsed lidar values agree reasonably well with independent assessments of extinction. The relative merit of instantaneous versus time-averaged signatures is discussed. The cw technique did not show the predicted visibility-dependence, apparently due to inadequate system sensitivity.

| 17. Key Words | 18. Distribution Statement |
|---|---|
| Lidar, Slant Visual Range, Low Visibility Measurements | DOCUMENT IS AVAILABLE TO THE PUBLIC THROUGH THE NATIONAL TECHNICAL INFORMATION SERVICE, SPRINGFIELD, VIRGINIA 22151. |

| 19. Security Classif. (of this report) | 20. Security Classif. (of this page) | 21. No. of Pages | 22. Price |
|---|---|---|---|
| Unclassified | Unclassified | 116 | |

Form DOT F 1700.7 (8-72) Reproduction of completed page authorized

## PREFACE

This report documents the experimental phase of a TSC program to assess the effectiveness of lidar in monitoring airport visibility. The report deals specifically with field tests of the TSC lidar carried out during the months of July, 1972 and May, 1973.

A separate report is to follow this one, summarizing the results of lidar visibility work both at TSC and at other centers, and evaluating the potential of lidar for slant visual range measurement in low visibility.

The author wishes to acknowledge the contribution of Messrs. H.C. Ingrao, M.A. Yaffee and M. Cartwright, who shared among them the tasks of designing and overseeing the fabrication of the lidar. Additional mention is due to Mr. Yaffee who was deeply involved in all phases of the experimental work.

The field tests at West Quoddy Head Light (Lubec, Maine) were made possible through the cooperation of the U.S. Coast Guard Southeast Harbor Command. Boatswain R. Marston was most helpful in providing an unusual amount of heavy fog as well as the comforts of home during our stay.

The Richmond Fog Chamber was made available through arrangements with NASA-Ames, which manages the facility, and Mr. D. Horning of the University of California at Berkeley. Particular thanks go to Mr. J. Jeffries and his co-workers (Northrup Services, Inc.) who operated the fog-chamber installation.

TABLE OF CONTENTS

## TABLE OF CONTENTS (CONT.)

## LIST OF ILLUSTRATIONS

## LIST OF ILLUSTRATIONS (CONT.)

## LIST OF ILLUSTRATIONS (CONT.)

## LIST OF ILLUSTRATIONS (CONT.)

## LIST OF SYMBOLS AND ABBREVIATIONS

| | |
|---|---|
| A | area of lidar receiver objective |
| c | speed of light |
| C | contrast |
| FWHM | full width at half maximum |
| f | 1) geometry function, f(R); 2) frequency |
| G,H | amplitudes of (in phase, out-of-phase) components of modulated lidar return signal |
| K | coaxial lidar geometry parameter |
| m | meter |
| MHz | megahertz |
| ma | milliamps |
| mrad | milliradians |
| nm | nanometers |
| nsec | nanoseconds |
| $P, P_o$ | optical power (radiant flux in watts) |
| ppm | pulses per minute |
| PRF | pulse repetition frequency |
| R | range, distance |
| $R_o$ | range at which initial overlap occurs, for bistatic geometry |
| SVR | slant visual range |
| str | steradian |
| t | time |
| T | transmission (%), over 19.2 meter baseline |
| $\overline{T}$ | average transmission |
| TIR | total internal reflection |

## LIST OF SYMBOLS AND ABBREVIATIONS (CONT.)

| | |
|---|---|
| TR | transient recorder |
| V | volts |
| $V_m$ | meteorological range (contrast threshold = .02); visibility |
| $V_{AB}$ | "visibility" between points A and B |
| WE | waveform eductor |
| $\beta(R)$ | volume backscatter coefficient |
| $\eta$ | quantum efficiency |
| $\theta$ | angle |
| $\theta_T$ | full divergence of transmitter beam, radians |
| $\theta_R$ | full receiver field-of-view, radians |
| $\lambda$ | wavelength |
| $\rho$ | ratio of signal amplitudes at two points on backscatter signature. |
| $\sigma(R)$ | extinction coefficient at range R |
| $\bar{\sigma}$ | average extinction coefficient |
| $\tau_p$ | laser pulse duration |
| $\phi$ | phase |
| $\omega$ | modulation frequency, $\omega=2\pi f$ |
| $\Omega$ | solid angle |

# 1. INTRODUCTION

For the past two years, the Optical Devices Group of the Electromagnetic Technology Division at TSC has been engaged in the design and construction of an experimental lidar apparatus. The lidar functions as an optical radar to probe the distributed backscattering properties of aerosols suspended in the atmosphere. The backscatter signals are related to the extinction coefficient and hence to visibility. As a single ended instrument (transmitter and receiver are co-located), the lidar is of potential use to the FAA for measuring visual range along or near the glide path of a landing aircraft.

The use of the backscatter signature of a reflected short optical pulse to determine atmospheric visibility was demonstrated by Brown.[1] Using a ruby laser as a source, Brown found that the visibility deduced from backscatter signatures compared reasonably well with that obtained from a nearby standard transmissometer. He noted that limitations in the alignment stability of the transmitter-receiver axes produced some systematic error. Equally significant, however, were the variations between two standard transmissometers, reading over the same period of time but separated slightly in space. Brown concluded that the backscatter signature (lidar) method can perform at least as well in determining visual range as the standard fixed baseline, double-ended transmission method during low and moderate visibility conditions. Subsequently, work at the Stanford Research Institute under R.T.H. Collis has furthered the development of the lidar technique, particularly with regard to signal processing and analysis.[2,3] In addition, the SRI

group has addressed the difficult but important problem of interpreting the backscatter signature under conditions where the extinction coefficient is non-uniform in space. They have demonstrated some success in this latter case, but the problem is by no means solved. Viezee et al.[3] have expressed confidence in the operational utility of lidar signals under some common types of inhomogeneous visibility conditions, based on a preliminary assessment of automatic data processing techniques.

Much of the lidar work performed to date has depended on high peak power (megawatt) laser sources. These sources, while useful for obtaining lidar data to correlate with visibility, are not regarded as operationally safe devices.

It seems preferable instead to employ sources with low peak power (~1 kwatt) but moderately high repetition rates. The advantage of the latter stems both from the increased eye safety and from the enhancement in data processing capability. Viezee et al.[3] have also discussed this point. Recently published work by Brown,[4] who used a 250 watt, fiber-coupled GaAs laser diode transmitter with a 5 kHz PRF, represents a successful demonstration of this approach.

The TSC lidar was conceived as an independent, FAA-sponsored attempt to assess the potential of the backscatter signature concept of visibility measurement. The apparatus was designed to incorporate three different laser sources and a common receiver. The sources include a ruby laser (peak power ~20 Mw), a gallium aluminum arsenide (GaAlAs) laser diode array (peak power = 300 w, max. PRF ≃ 500 Hz), and a modulated continuous wave (helium-neon) laser. The reasons for including two pulsed sources were several.

On the one hand, the purpose of the work is to assess the feasibility of backscatter techniques in measuring visibility, and thus, it was considered necessary to examine both types of sources and to compare their performance.

In addition, because of considerations expressed above, it seemed likely that the only kind of system ultimately acceptable would have a low peak power but moderate average power output. This strongly favors using the diode laser (GaAlAs) array, and it was intended that the ruby source be used as a "bridge" to normalize the GaAlAs results with the previously reported high peak power lidar results. [These comments are not intended to exclude the possible application of eye safe high peak power sources, such as the erbium laser. At the time the present effort began, the erbium laser was at an early stage of development, compared to laser diode sources. Recently, an erbium laser ceilometer has been shown to give results very much comparable to the ruby laser ceilometer.[5]]

The inclusion of a third source in the present work is based on a technique suggested at TSC by Schappert.[6] This involves the use of a CW laser beam, modulated at RF frequencies. The phase of the reflected signal is compared with the phase of the outgoing beam. According to Schappert, the relative phase is a strong function of modulation frequency for a given visibility.

After a discussion in Section 2 of the theory underlying both pulsed and modulated CW lidars, a description is given of the TSC lidar instrumentation (Section 3). Each of the three systems will be discussed in turn. Several field tests have been conducted in the course of this program and they are outlined in Section 4.

The results of these, with regard to both system performance and visibility measurement, and conclusions based largely on the tests are also presented in that section.

# 2. THEORY

## 2.1 PULSED LIDAR

The optical signal power P(t) due to a time-dependent lidar pulse backscattered from the atmosphere is given by[7]

$$P(t) = A \int_o^\infty \frac{dR}{R^2} f(R)\ \beta(R) P_o(ct-2R) \exp\left(-2 \int_o^R \sigma(R')dR'\right). \qquad (2\text{-}1)$$

This equation expresses the fact that a signal from range R arriving at the receiver (area A) at time t corresponds to the laser output power $P_o$ at time t-2-R/c, where c=speed of light. The volume backscatter coefficient, $\beta$, and the extinction coefficient $\sigma$ are in general functions of range.

The function f(R) describes the geometrical and optical features of a specific lidar which cause the receiving efficiency to vary with range. This includes overlap of receiver and transmitter cones of view, for bistatic systems, and obscuration by reflecting components in coaxial systems. Losses at the field aperture due to range-dependent defocusing also are included in f(R).

Several approximations to eq. (2-1) are useful. First, if the outgoing light is from a laser with pulse width ($c\tau_p$) short compared to distances over which f(R), $\beta$(R) and the exponential attenuation vary significantly, the return power can be written

$$P(t=\frac{2R}{c}) = A\ \beta(R)\ \frac{c\tau_p}{2}\ \frac{f(R)}{R^2}\ \exp\left(-2 \int_o^R \sigma(R')dR'\right) . \qquad (2\text{-}2)$$

If the atmospheric aerosol is uniformly distributed, this expression takes the form

$$P(t=\frac{2R}{c}) = A\ \beta\ \frac{c\tau_p}{2}\ \frac{f(R)}{R^2}\ e^{-2\sigma R} \quad . \qquad (2\text{-}3)$$

The short pulse approximation above is not sufficiently accurate for many purposes. For example, in the present work, the full width at half maximum of the GaAlAs laser pulse was greater than 100 ns. Variations in f(R) and attenuation over distances of 50-100 ft. are significant, especially for values of $R \lesssim$ 100-200 ft. and visibilities under 1200 ft. It is necessary in such cases to take account of the finite shape of the outgoing laser pulse. Eq. (2-1) can be transformed to exhibit a convolution over the shape of the laser pulse in time:

$$P(R) = \frac{Ac}{2} \int_{t}^{t+\tau_p} P_o(\tau) f\left(R-\frac{c\tau}{2}\right) \frac{\beta\left(R-\frac{c\tau}{2}\right) \exp\left(-2\sigma\left(R-\frac{c\tau}{2}\right)\right)}{\left(R-c\tau/2\right)^2}\, d\tau, \qquad (2\text{-}4)$$

where $t = \frac{2R}{c}$ . The time $\tau_p$ may be larger than the pulse width at half-maximum and represents the duration over which the pulse has "significant" amplitude. As can be seen from Fig. 1, it is important to use Eq. (2-4) to treat data obtained with large pulse width systems, particularly when making computations for $R \lesssim c\tau_p$. Obviously one would prefer sources with the shortest pulse widths possible, consistent with the resolution of the overall lidar system.

### 2.1.1 Computation of the Extinction Coefficient

The received backscattered power incident on the detector ultimately produces a display which is a known function of P(t). From this function, it is possible to deduce the variation of extinction coefficient with range leading to estimates of the

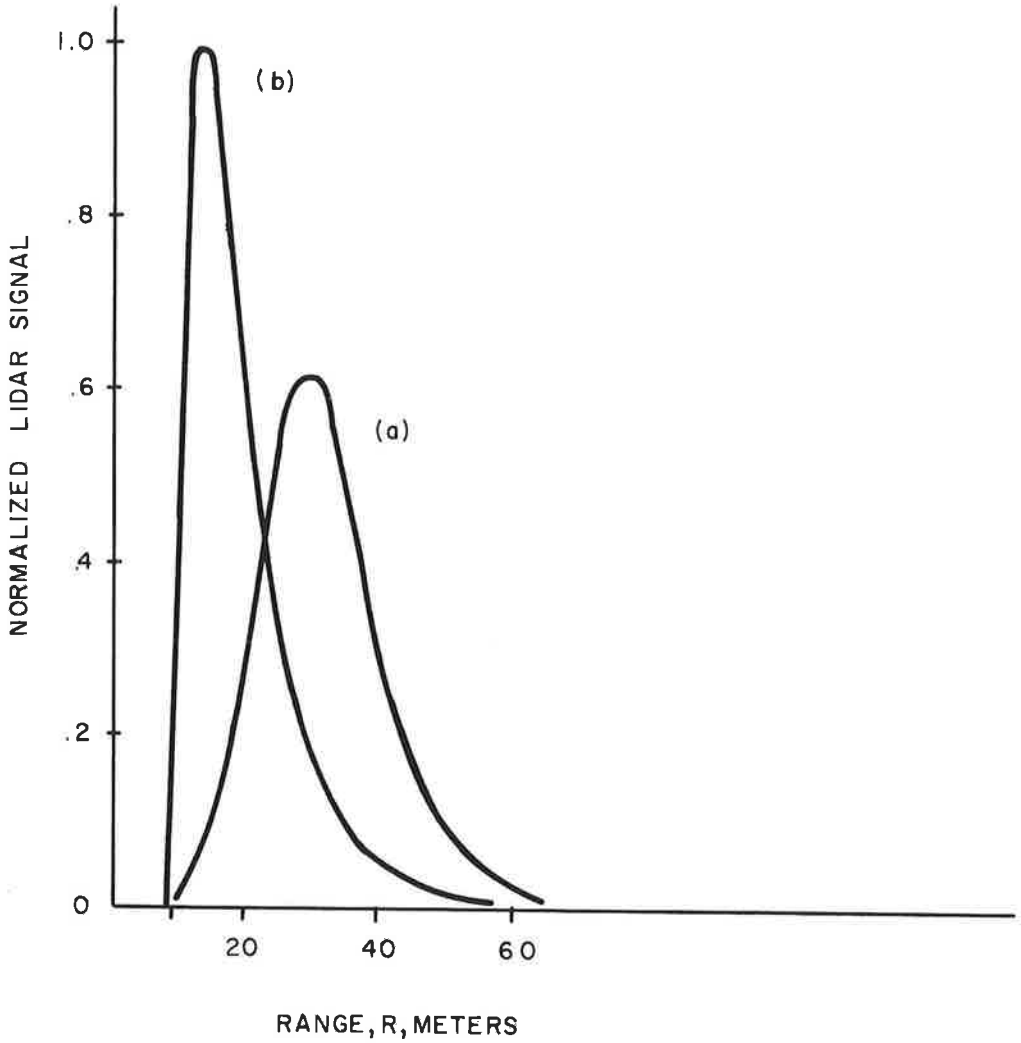


Figure 1. Computed lidar signals for (a) finite Gaussian pulse (FWHM = 90 nsec), and (b) idealized short pulse (delta function). Signals are based on a standard visibility, $V_m$, of 300 meters and overlap parameter $R_o$=10 meters. Pulses are normalized to the same total energy

visibility through selected portions of space. In the present work, the computations are based directly on return signals proportional to P(R) $\left(R=\frac{ct}{2}\right)$. Others have used analog preprocessing methods, such as range-squared multiplication[4] and logarithmic amplification[3], to reduce the computational burden.

The instantaneous backscattered power received at the detector depends on both the backscatter coefficient $\beta$ and the extinction coefficient $\sigma$ (see Eq. 2-1). For the kinds of aerosols of interest in low visibility (i.e., water droplets) and for wavelengths in the visible or near-infrared, Mie scattering is predominant. In order to make quantitative use of the amplitude of the lidar signal to determine the extinction coefficient, one would need a relationship between $\beta$ and $\sigma$. In general, such a relationship depends strongly on the density, the refractive index and the size distribution of the particles, as well as on the spectral distribution of the light involved. While an empirical relation has been found for $\beta$ and $\sigma$, of the form,[8] $\sigma = k_1 \beta^{k_2}$ with $k_2 \approx 1.5$, this is generally considered to be unreliable for monochromatic light[9] where the dependence of Mie scattering on (unknown) size distributions is emphasized.

Methods have been developed to extract the extinction coefficient from the lidar signal without depending on a precise knowledge of $\beta/\sigma$. Brown[1] first made use of the shape (or "signature") of the lidar signal, showing that information about atmospheric extinction can be deduced from measurement of such parameters as the width of the signal and the distance to the peak. However, these parameters were found to be undesirably affected by lidar alignment stability and geometry factors;

furthermore they could only be used in strictly homogeneous conditions.

More recently, two methods have been in use which permit analysis, with certain restrictions, even in inhomogeneous fog. In the "slope" method[3] the data are processed to compute the so-called "S-function", which can be written as

$$S(R) = \ln \left[ \frac{R^2 P(R)}{f(R)} \right] + \text{constant.} \qquad (2\text{-}5)$$

Based on Eq. (2-3) for homogeneous fog, the range-averaged value of atmospheric extinction coefficient $\bar{\sigma}$ is

$$\bar{\sigma} = -\ 1/2\ \frac{\Delta S}{\Delta R}\ . \qquad (2\text{-}6)$$

To use this method, one first determines, from the behavior of the S-function, regions of space in which the slope is reasonably constant. For each such region, a least squares computation is made to find the average slope. The use of the slope method is discussed in more detail in reference 3.

Another method, sometimes referred to as the "ratio" method,[4] appears to be especially advantageous in analyzing inhomogeneous conditions. The range is broken up into intervals $\Delta R_i$. In practice intervals may range from 10 to 50 feet. The average extinction coefficient $\sigma_i$ over interval i is

$$\sigma_i = \frac{1}{2\Delta R_i} \ln \left[ M_i \frac{\beta(R_{i+1})}{\beta(R_i)} \right] \qquad (2\text{-}7)$$

where $\Delta R_i \equiv R_{i+1} - R_i$,

$$M_i \equiv \frac{R_i^2 \, P(R_i) \, f(R_{i+1})}{R_{i+1}^2 \, P(R_{i+1}) \, f(R_i)} \, .$$

If the intervals are taken sufficiently close together, the variation in $\beta$ over successive intervals can be ignored, and this leads to the useful approximation

$$\sigma_{\Delta R_i} = \frac{1}{2\Delta R_i} \ln M_i \, . \qquad (2\text{-}8)$$

The term "visibility", as used in this report, refers to the commonly used meteorological range, $V_m$. This is the distance, under daylight conditions, at which the contrast of a target (whose initial contrast against the background is unity) is reduced to .02. Expressed mathematically, the contrast C of the target as seen from a distance R is assumed to vary according to $C=C_o \exp(-\sigma R)$, with $C_o=1$.

Since $R=V_m$ when $C=.02$, it is seen that the visibility $V_m$ is related to extinction coefficient $\sigma$ by*

$$V_m = \frac{3.91}{\sigma} \, . \qquad (2\text{-}9)$$

The choice of C=.02 for the contrast threshold was first proposed by Koschmieder and equation (2-9) is frequently referred to as Koschmieder's law.[10] The visibility between points A and B can be found from the average extinction coefficient $\bar{\sigma}_{AB}$ as $V_{AB}=\frac{3.91}{\bar{\sigma}_{AB}}$, where

$$\bar{\sigma}_{AB} = \frac{1}{N} \left[ \sum_{R_A}^{R_B} \sigma_{\Delta R_i} \right] \qquad (2\text{-}10a)$$

*Effects due to wavelength are omitted, the expression being strictly correct only for $\lambda=.55\mu$. However, at low visibilities (<1000 ft.) and in the visible and near IR, these effects are small (<10-15%).

and

$$N = \frac{R_B - R_A}{\Delta R} \quad . \tag{2-10b}$$

The measured value of $\sigma$ can also be used to compute the visibility of lights, via Allard's law.[10] In this connection it should be emphasized that lidar-obtained knowledge of $\bar{\sigma}$ is at least equivalent to transmissometer measurements over the same path and, because of the range-resolving feature, contains more potentially useful information.

In a sense, the philosophy of the slope method is opposite to that of the ratio approach. In the former case, since a least-squares fit to the data is involved, the baseline $\Delta R$ must be large enough to be representative of the whole range considered. Otherwise, local inhomogenities may be given undue weight.

The ratio method, on the other hand, strives to obtain reasonably accurate measurements over a number of relatively small intervals. It will be shown below that, in order to obtain a given accuracy in the extinction coefficient using the ratio method, the required accuracy of the raw data increases as smaller intervals $\Delta R_i$ are chosen.

It remains to be seen which of these approaches is most useful. It is likely that the choice will depend not only on the principle of the calculational approach, but also on the ease with which either method can be adapted to automatic signal processing.

### 2.1.2 Computer Analysis of Data

The reduction of data from the TSC pulsed lidars has been treated several ways. The handling of the finite laser pulse width was made possible by an adaption of the ratio method to a

computer-implemented iterative procedure which will now be outlined. (This procedure was developed for TSC by Radiation Research Associates, Inc., Fort Worth, Texas. The Fortran program listing, and additional information are given in Appendix A.)

The starting point of the computation is eq. (2-4). The ratio $\rho$ of return powers from two successive values of R is formed.

$$\rho_i \equiv \frac{P(R_i)}{P(R_{i+1})} = \left[\int_o^{\tau_p} d\tau P_o(\tau) z_i^{-2} f(z_i) e^{-2\sigma z_i}\right] \cdot \left[\int_o^{\tau_\rho} d\tau P_o(\tau) z_{i+1}^{-2} f(z_{i+1}) e^{-2\sigma z_{i+1}}\right]^{-1} \qquad (2\text{-}11)$$

where $z_i = R_i - c\tau/2$. The variation of $\beta$ over successive intervals has been ignored. Experimental data consisting of pairs of values $[P(R_i), R_i]$ are digitized and input to a PDP-10. The program determines ratios $\rho_i$ for successive intervals $\Delta R_i$. A starting test value is selected for $\sigma = \sigma_{si}$ and used to calculate $\rho_{si}$. Next $\sigma_i$ is incremented slightly and the process is repeated until $|(\rho_i - \rho_i')| \to 0$, such that successive test values of $\sigma_i$ satisfy

$$\frac{|\sigma_i - \sigma_i'|}{\sigma_i} \leq 0.1$$

(for 10% "accuracy"). The final value of $\sigma_i$ is printed out. At the same time, $\sigma_i$ is calculated as if the pulse width were negligible, so the values can be compared. Finally, the average $\bar{\sigma}_{AB}$ is obtained from eq. (2-10).

### 2.1.3 Errors in σ Related to Measurement of Backscattered Power P(R)

It is informative to estimate the error in σ (and ultimately in visibility) arising from uncertainty in measured quantities. We choose two values of $R(R_1,R_2)$ on the decreasing side of the lidar signal, with measured return powers corresponding to $P_1$ and $P_2$. We can write

$$\rho = \frac{P_1}{P_2} = \frac{f(R_1)\ R_2^2\ e^{-2\sigma(R_1-R_2)}}{f(R_2)\ R_1^2}$$

and

$$\ln\ \rho = \ln\left(\frac{f(R_1)R_2^2}{f(R_2)R_1^2}\right) + 2\sigma(R_2-R_1).$$

Differentiating,

$$\frac{d\rho}{\rho} = 2\Delta R d\sigma = 2\sigma\Delta R\left(\frac{d\sigma}{\sigma}\right),$$

where $\Delta R = R_2 - R_1$.

Rewriting the above equation gives

$$\frac{d\sigma}{\sigma} = \frac{1}{2\sigma\Delta R}\left[\frac{dP_1}{P_1} - \frac{dP_2}{P_2}\right] \quad . \qquad (2\text{-}12)$$

Some important features of eq. (2-12):

a) The larger the interval ΔR, the more accurately the slope can be determined and hence the smaller error in measuring σ. (Of course, if ΔR is taken arbitrarily large, inhomogenities may be overlooked.)

b) The better the visibility, the larger the <u>percentage</u>

error in the measurement of visibility, for given $\Delta R$ and dP's. This is a consequence of the shallower slope of the lidar signal as visibility improves.

c) Uncertainty in P(R) due to random noise can give either positive or negative values for $dP_1$, $dP_2$. However, systematic errors (such as drifting zero level) would tend to give $dP_1$ and $dP_2$ the same sign. Hence, to some extent, systematic errors in reading P will cancel.

d) Ultimately, the values of $dP_1$, $dP_2$ will depend on the signal-to-noise ratio.

## 2.2 MODULATED CW LIDAR

Schappert[6] has proposed a technique for determining the visibility from the phase (or amplitude) relations between an outgoing modulated laser beam and the backscattered light. The present TSC experimental arrangement does not make use of the harmonic relationships suggested by Schappert.[6] Instead, the outgoing intensity has a sinusoidally-varying component at frequency f:

$$P_{out} = P_o \sin \omega t \qquad \text{where } \omega = 2\pi f.$$

The return power at frequency $\omega$ is obtained, using eq. (2-1),

$$P^{\omega}(t) = A\beta P_o \int_o^{\infty} dR f(R) e^{-2\sigma R} \sin \omega(t-2R/c), \qquad (2\text{-}13)$$

where $\beta$ and $\sigma$ are taken to be independent of R. The present calculation then applies only to homogeneous atmospheres.

Expanding (2-13)

$$P^{\omega}(t) = G(\omega) \sin \omega t - H(\omega) \cos \omega t \qquad (2\text{-}14)$$

where

$$G(\omega) = A\beta P_o \int_o^\infty \frac{dRf(R)e^{-2\sigma R}}{R^2} \cos \frac{2\omega R}{c} \qquad (2\text{-}14a)$$

and

$$H(\omega) = A\beta P_o \int_o^\infty \frac{dRf(R)e^{-2\sigma R}}{R^2} \sin \frac{2\omega R}{c} \qquad (2\text{-}14b)$$

Rewriting (2-14)

$$P^{\omega}(t) = a(\omega) \sin\left(\omega t - \phi(\omega)\right) , \qquad (2\text{-}15)$$

where

$$a(\omega) = \sqrt{G^2(\omega) + H^2(\omega)} \qquad (2\text{-}15a)$$

and

$$\phi(\omega) = \tan^{-1} H(\omega)/G(\omega) . \qquad (2\text{-}15b)$$

Using the above relationships, the phase $\phi(\omega)$ was computed as a function of frequency, for several lidar geometries. (The functional forms which describe the lidar geometry are defined in the next section.) Figure 2 shows the behavior of $\phi(\omega)$ for a visibility of 650m. The dramatic break in the phase curve, where the slope approaches $-\infty$, occurs at a distinct frequency $f_o = \frac{\omega_o}{2\pi}$. Figure 3 shows the theoretical dependence of $f_o$ on visibility. This is the basis for the instrumental application of the technique.

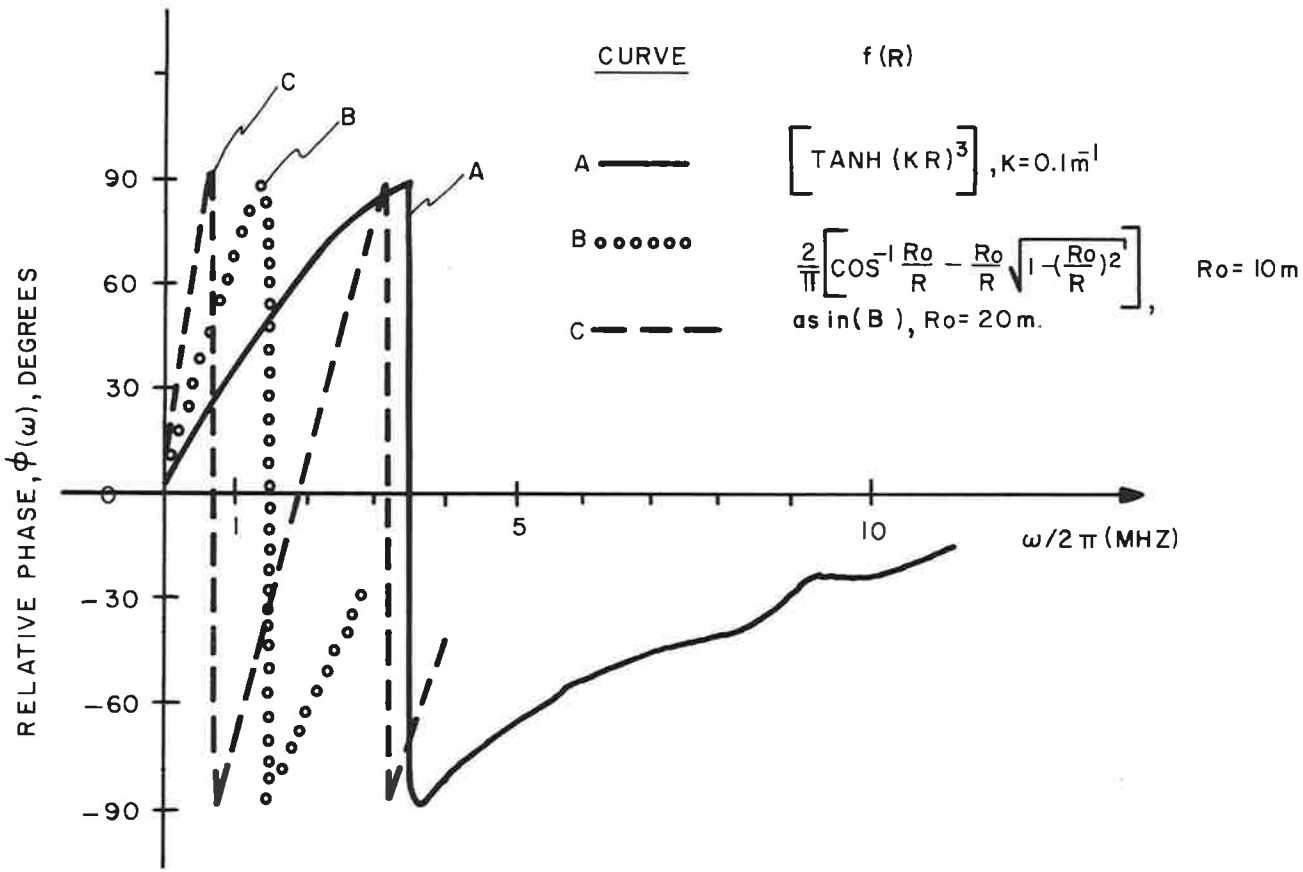


Figure 2. Relative phase $\phi(\omega)$ of modulated CW lidar return as a function of the modulation frequency $\omega/2\pi$. Curve (a) coaxial geometry; (b), (c) bistatic systems. The function $\phi(\omega)$ is defined by eqs. (2-15) in text. The visibility used for the calculation is 650 meters [The functions f(R) are defined in eqs. (2-16) and (2-17) in text.]

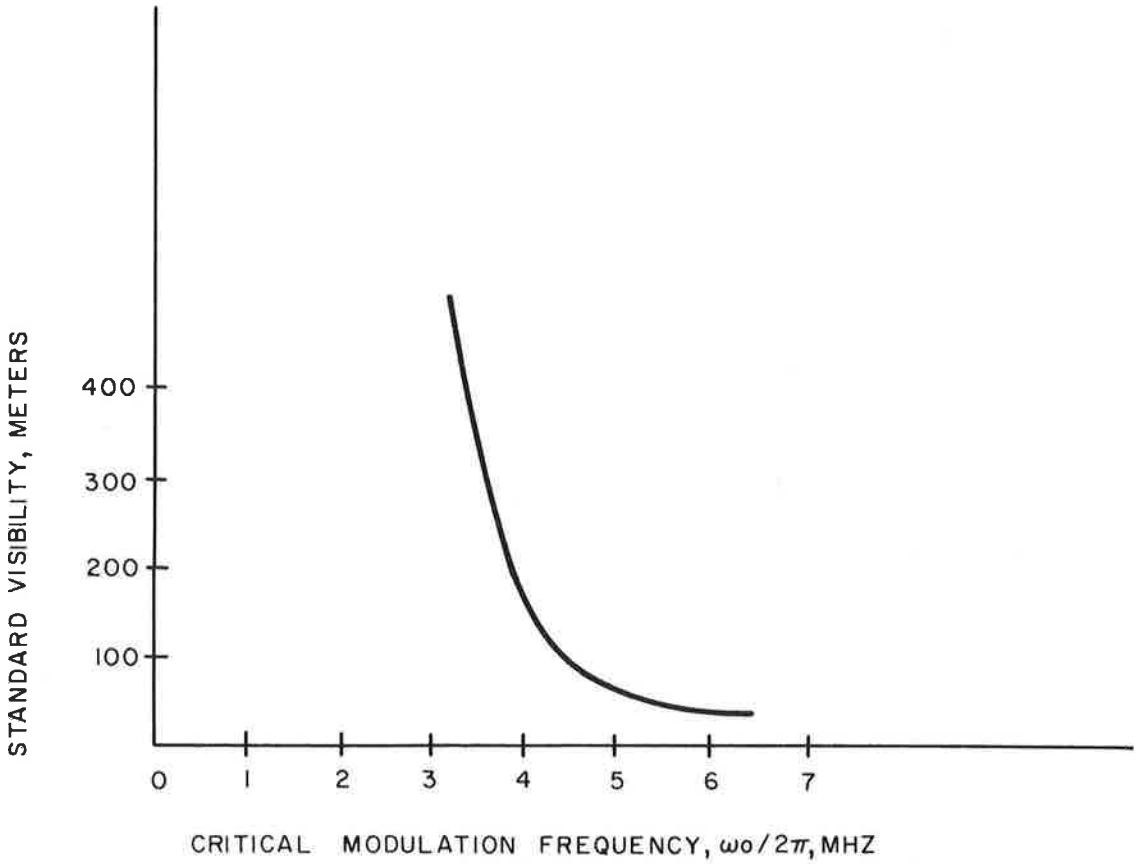


Figure 3. Theoretical relation between standard visibility and critical modulation frequency ($\omega o/2\pi$), for a coaxial geometry with $f(R) = [\tanh(KR)]^3$, $K=0.1m^{-1}$ [See eq. (2-15)]

## 2.3 FUNCTIONAL REPRESENTATION FOR THE LIDAR GEOMETRY

As has been mentioned above, the optical "efficiency" of a lidar is a function of target range. This is due to effects such as incomplete beam overlap, defocusing and vignetting at the field aperture due to finite target distance, and partial obscuration by optical components. The two types of lidar geometry used most frequently, each of which is represented in the TSC system to be discussed later in this report, are shown in Figure 4.

For the bistatic system,[7] with the beams intersecting at $R_o$, and with $\theta_T = \theta_R$,

$$f(R) = \frac{2}{\pi}\left[\cos^{-1}\frac{R_o}{R} - \frac{R_o}{R}\sqrt{1-\left(\frac{R_o}{R}\right)^2}\right] \quad R > R_o \qquad (2\text{-}16)$$
$$= 0 \quad R \leq R_o.$$

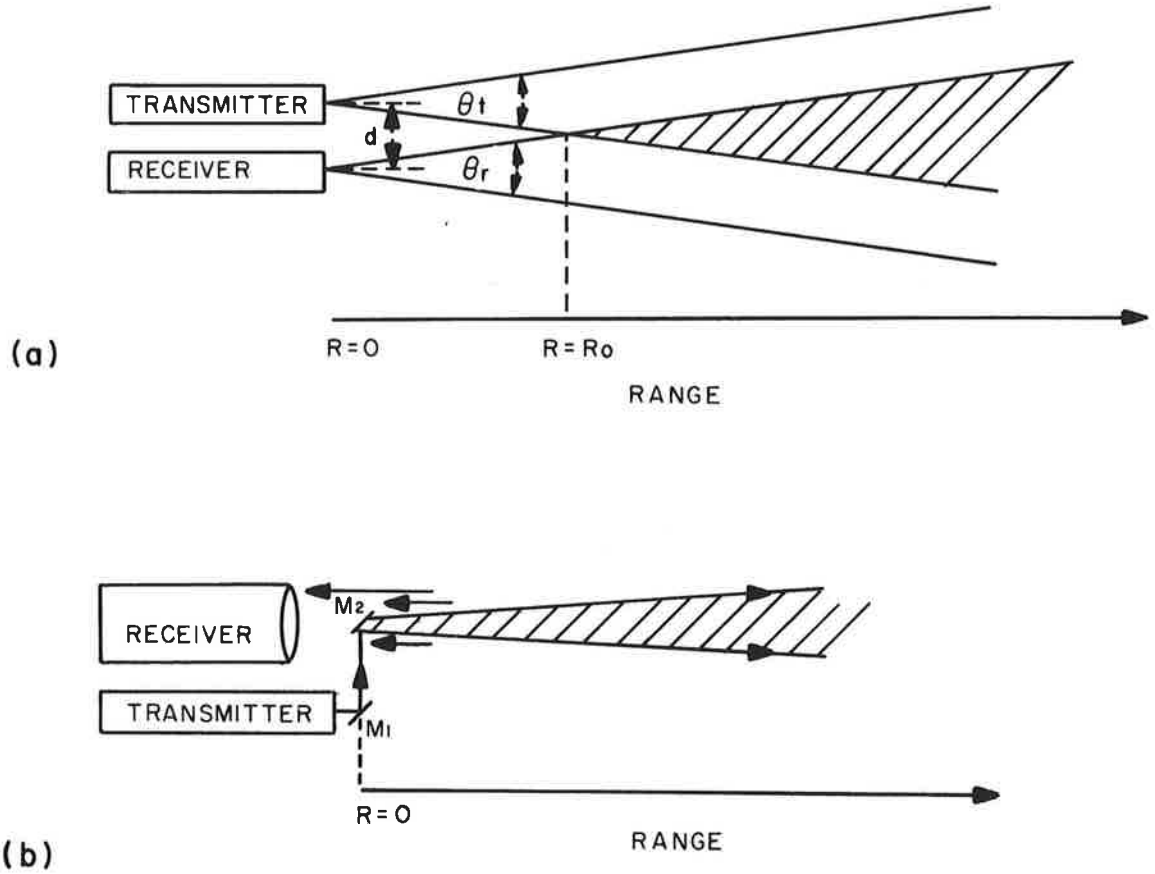


Figure 4. Two lidar geometries: (a) Bistatic arrangement, $\theta_T = \theta_R$; (b) coaxial arrangement with reflectors $M_1$, $M_2$ to align beam axes

The function f(R) increases from 0 to unity as the beam overlap becomes complete. It is this function which competes with the term $R^{-2}e^{-2\sigma R}$ to cause the appearance of a peak in the lidar signal whose position depends on the values of $R_o$ and $\sigma$.

It is no doubt also possible to represent the obscuration and defocusing effects for a coaxial lidar in a closed functional form. However, it is convenient to use a general function for f(R) which has the proper qualitative behavior and then fit the free parameter empirically. The form chosen is

$$f(R) = \left[\tanh\,(KR)\right]^3 \quad . \tag{2-17}$$

It will be noted that for small values of R, $f(R) \propto R^3$. This obviates the calculational problem that otherwise would arise from the $R^{-2}$ term near R = 0.

Figure 5 shows the behavior of the geometry functions for bistatic and coaxial systems, as calculated from equations (2-16) and (2-17). Experimental verification of the representative validity of these functions is discussed in Section 3.

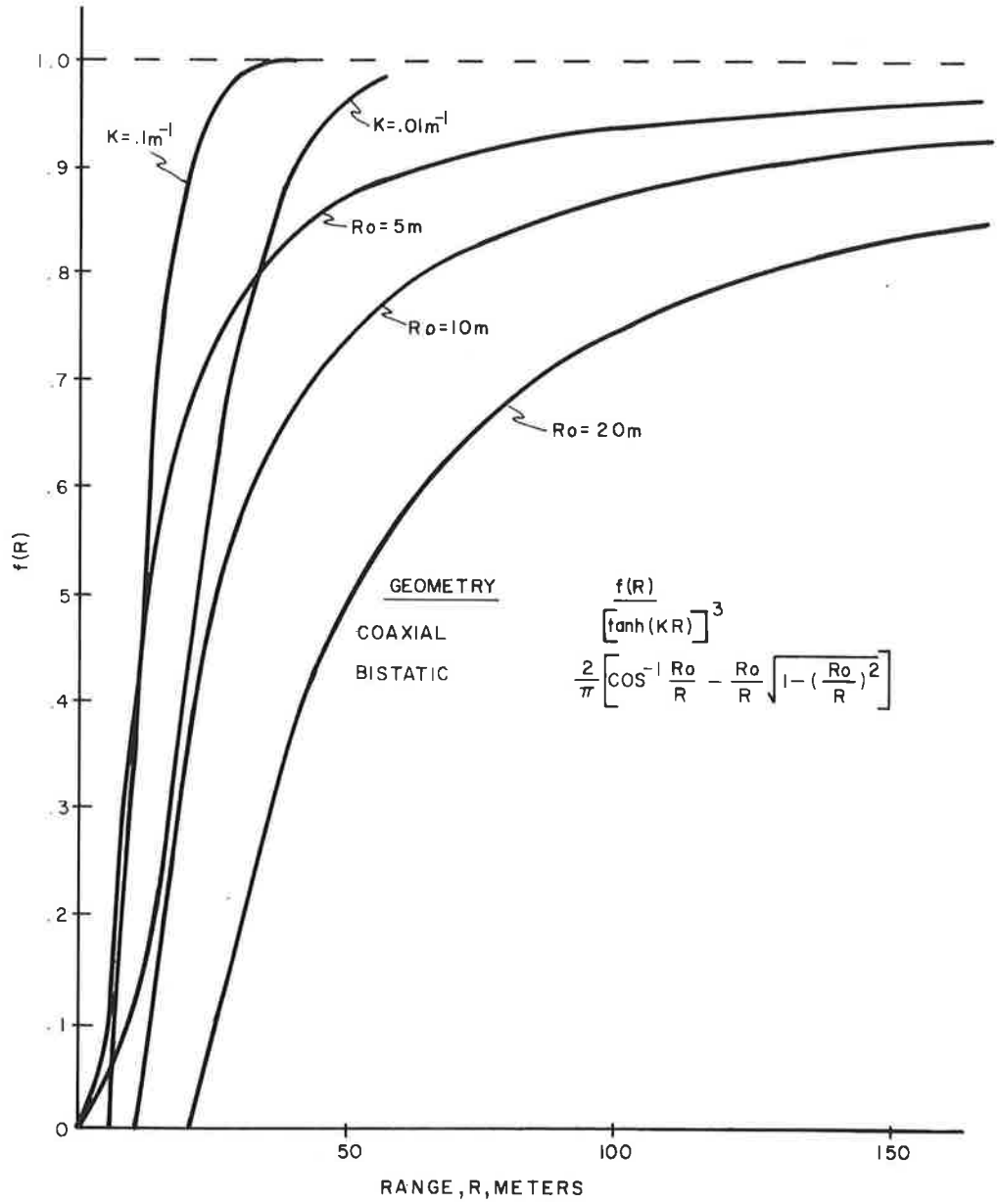


Figure 5. Geometrical function f(R) vs range R, for bistatic and coaxial lidars

# 3. TSC LIDAR: INSTRUMENTATION

This section is devoted to a description of the instrumental details of the TSC lidar. The components of this lidar system were designed with the intention of determining the feasibility of visibility measurements. As a result, the system has served a largely experimental function. Although ruggedly built, the present lidar has few specific features on which to model a future prototype system. For this reason, only those instrumental details will be included which bear on system operation or the interpretation of results. The TSC lidar consists of three transmitters, housed in separate modular "drawers" and a receiver (telescope, optical filters and detector) housed in a fourth module.

The four modules are of identical dimensions (8"x8"x36") and slide individually into guide channels of a rectangular frame box. Figures 6-11 show the lidar main frame and the separate module drawers. The altazimuth mount allows the "point angle" of the lidar to be varied in elevation from below the horizon to the zenith, while the entire range of azimuth angles can be covered. The individual transmitter systems are described below.

## 3.1 GALLIUM ALUMINUM ARSENIDE LIDAR

### 3.1.1 Laser Source

The gallium aluminum arsenide (GaAlAs) laser transmitter* was made by TCS Advanced Technology Laboratories, Burlington, MA, and

*The center wavelength is adjusted by the amount of aluminum added to the diode material. Pure GaAs emits at around 9050Å. The reason for the additional aluminum is to provide a shorter wavelength to take advantage of the increased PMT sensitivity.

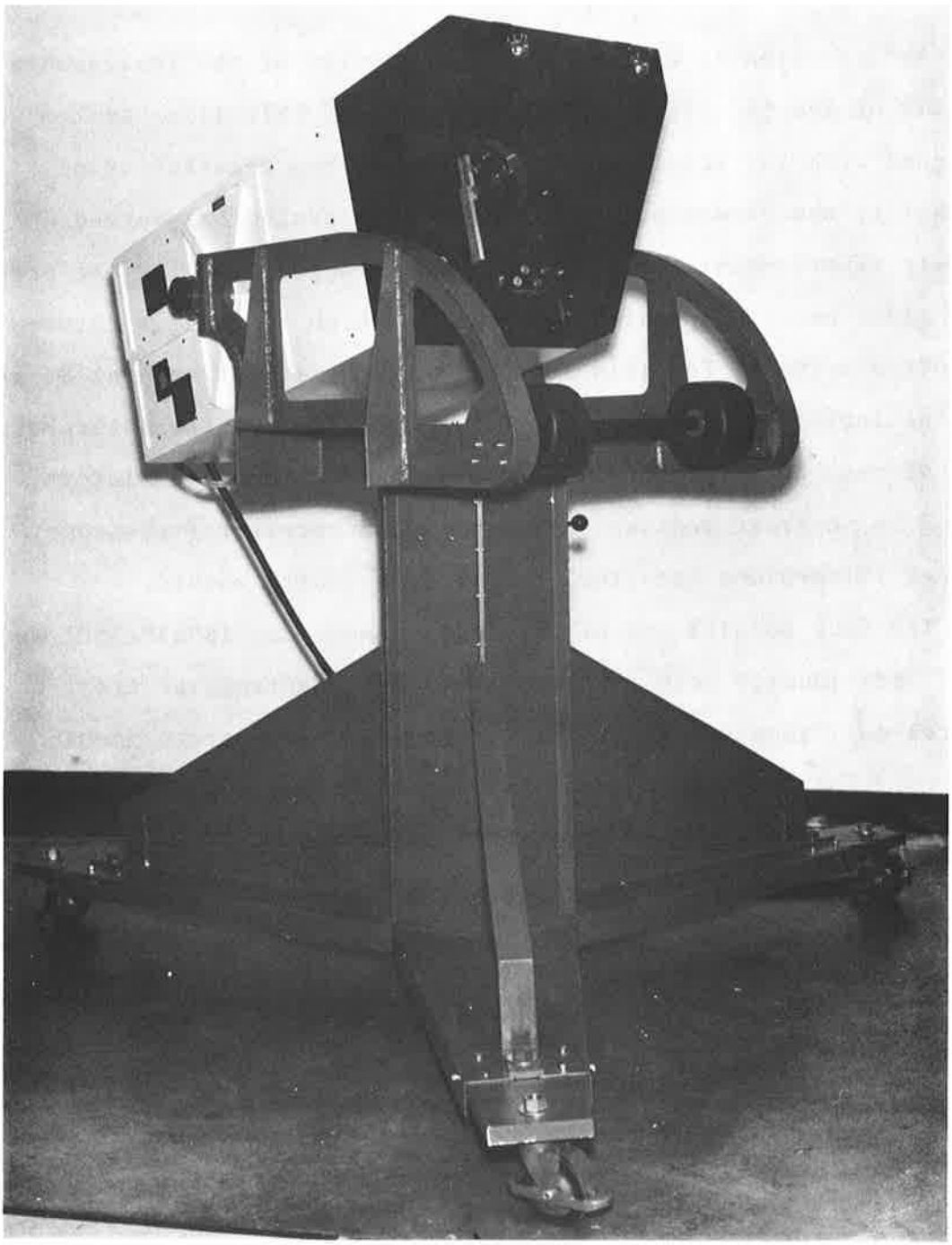

Figure 6. TSC multiple unit lidar

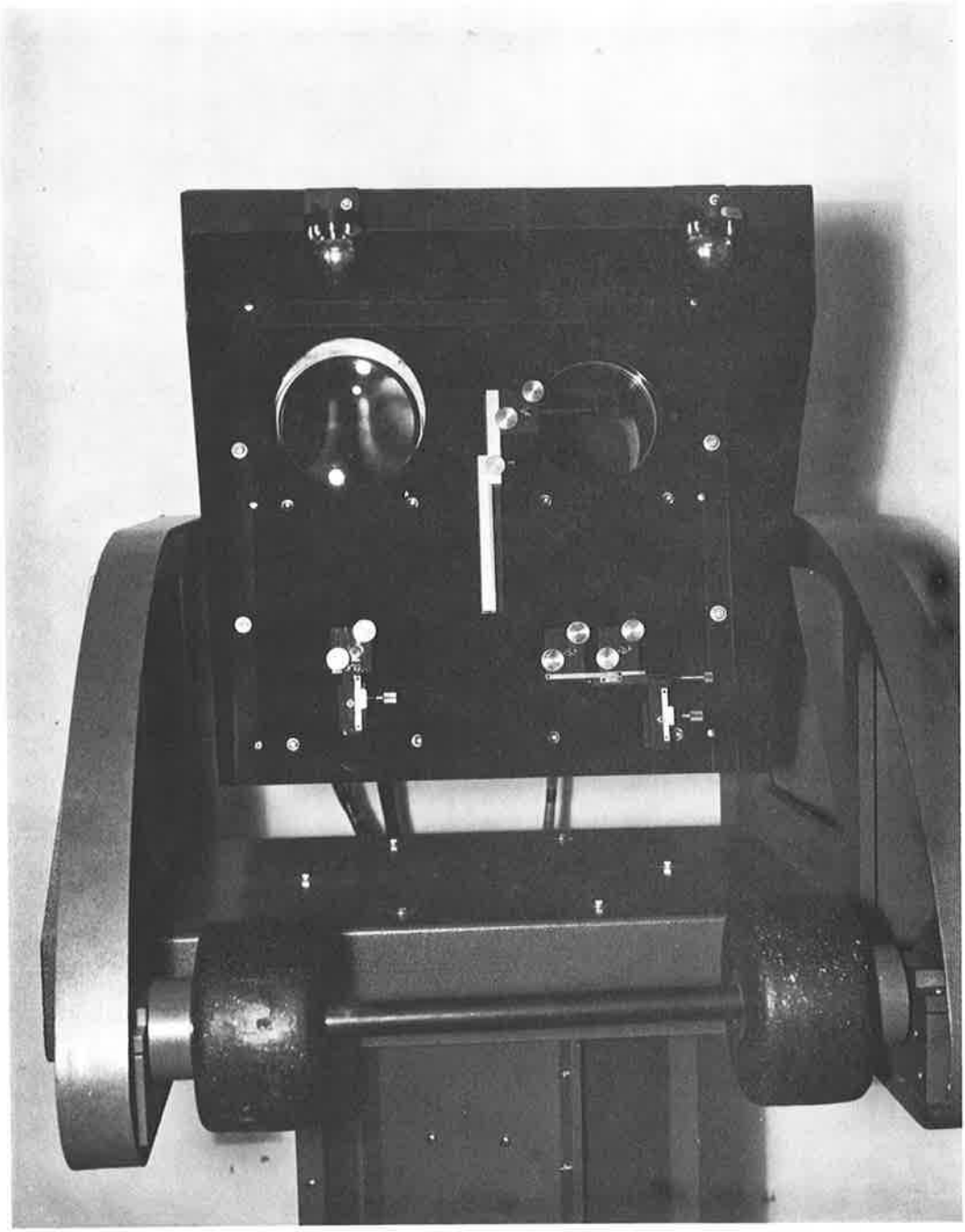

Figure 7. Closeup of source-receiver optics. Large lens at left belongs to GaAlAs transmitter. At right, the receiver lens, common to all systems. Near center of receiver lens is one of pair of beam-directing prisms which permit ruby beam (lower right) to be coaxial with receiver axis. Helium-neon laser source (lower left) can be directed similarly

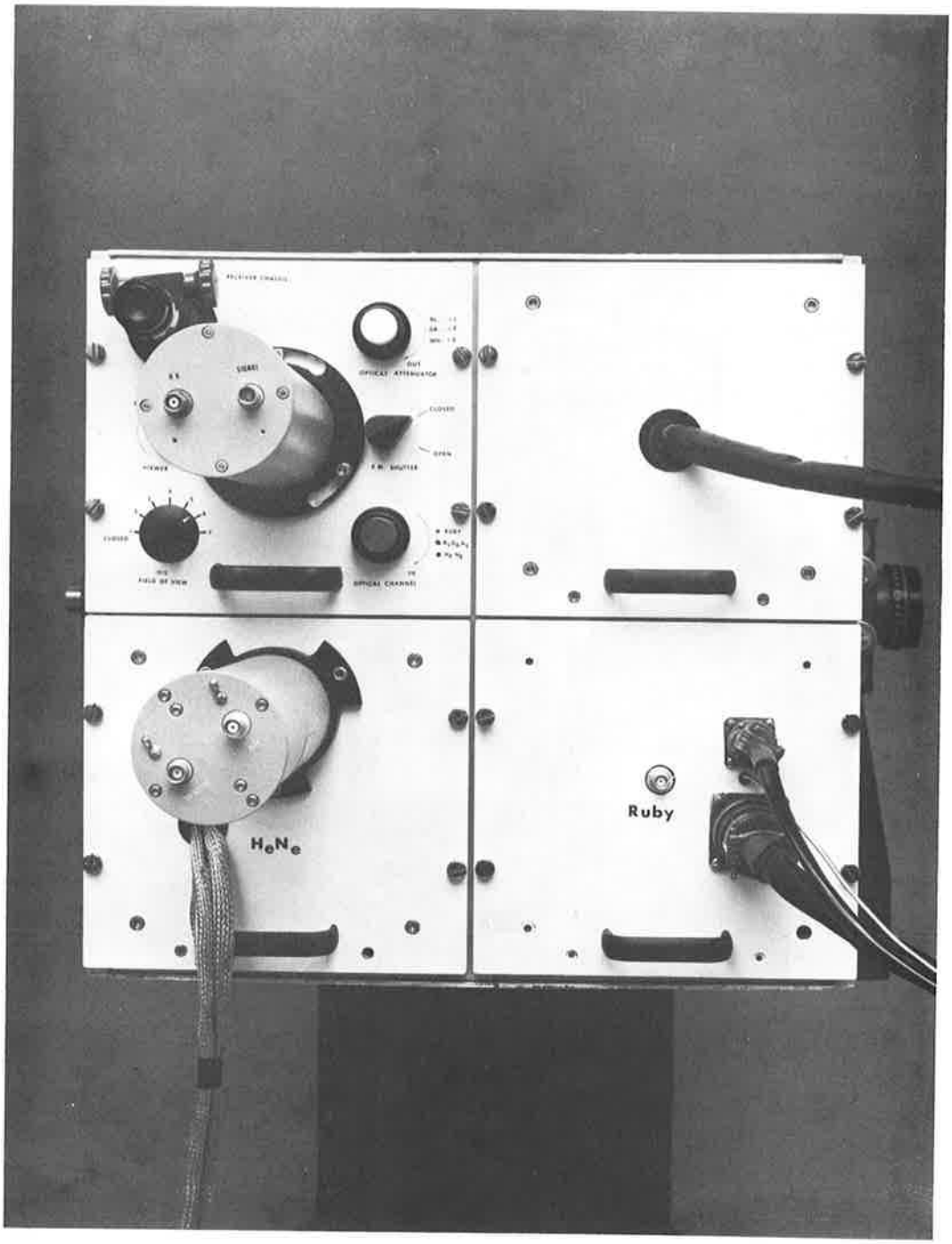


Figure 8. Rear view of lidar enclosure. Photomultiplier housings belong to receiver (top) and reference channel for CW modulation lidar (bottom left). The unlabeled panel at top right houses the GaAlAs transmitter

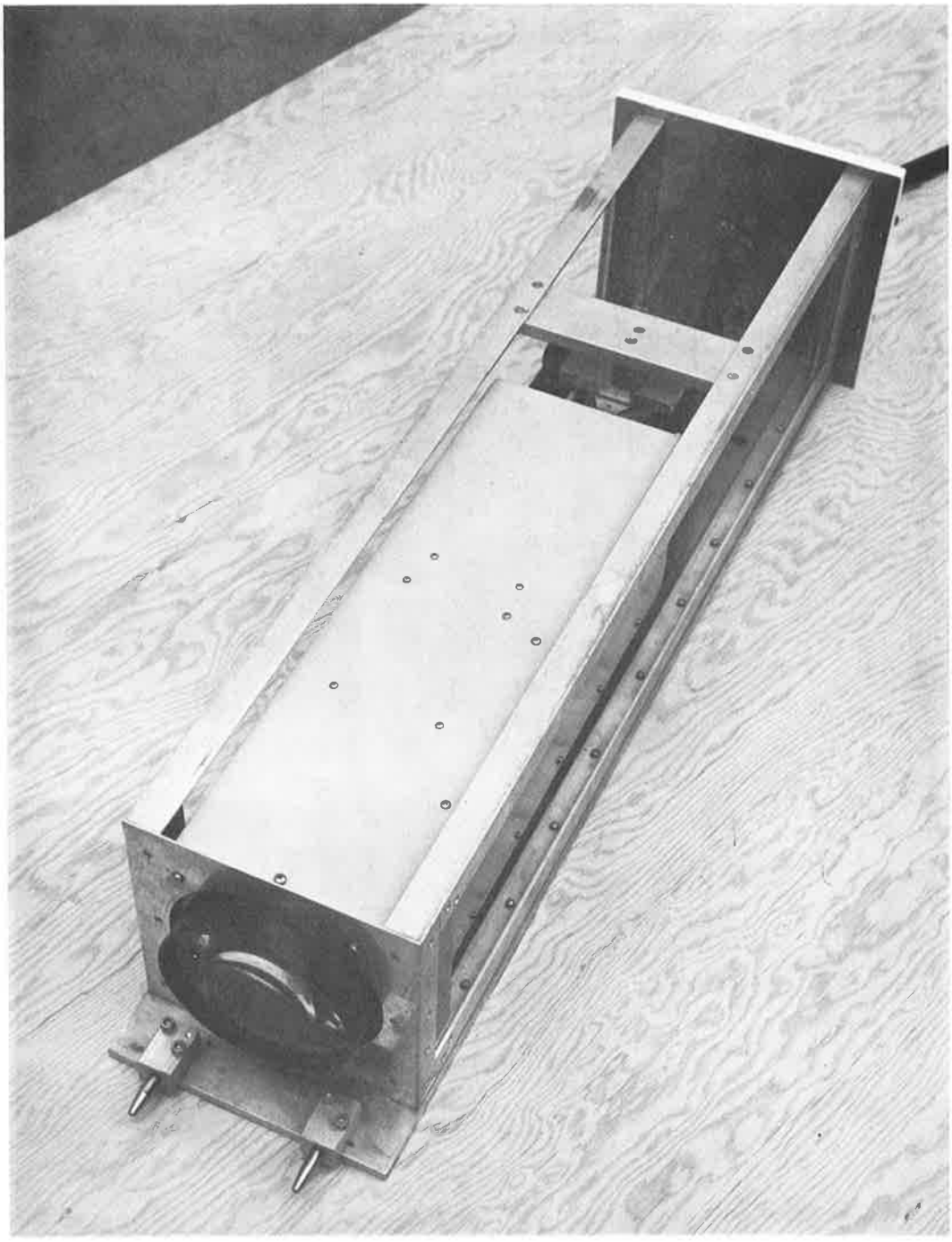

Figure 9. Module containing GaAlAs transmitter. Enclosure is 20" x6"x6" and houses laser diode array, optical integrator, drivers, thermoelectric temperature controller and power supplies (300 VDC and 6 VDC). Rack-mounted control panel is separate

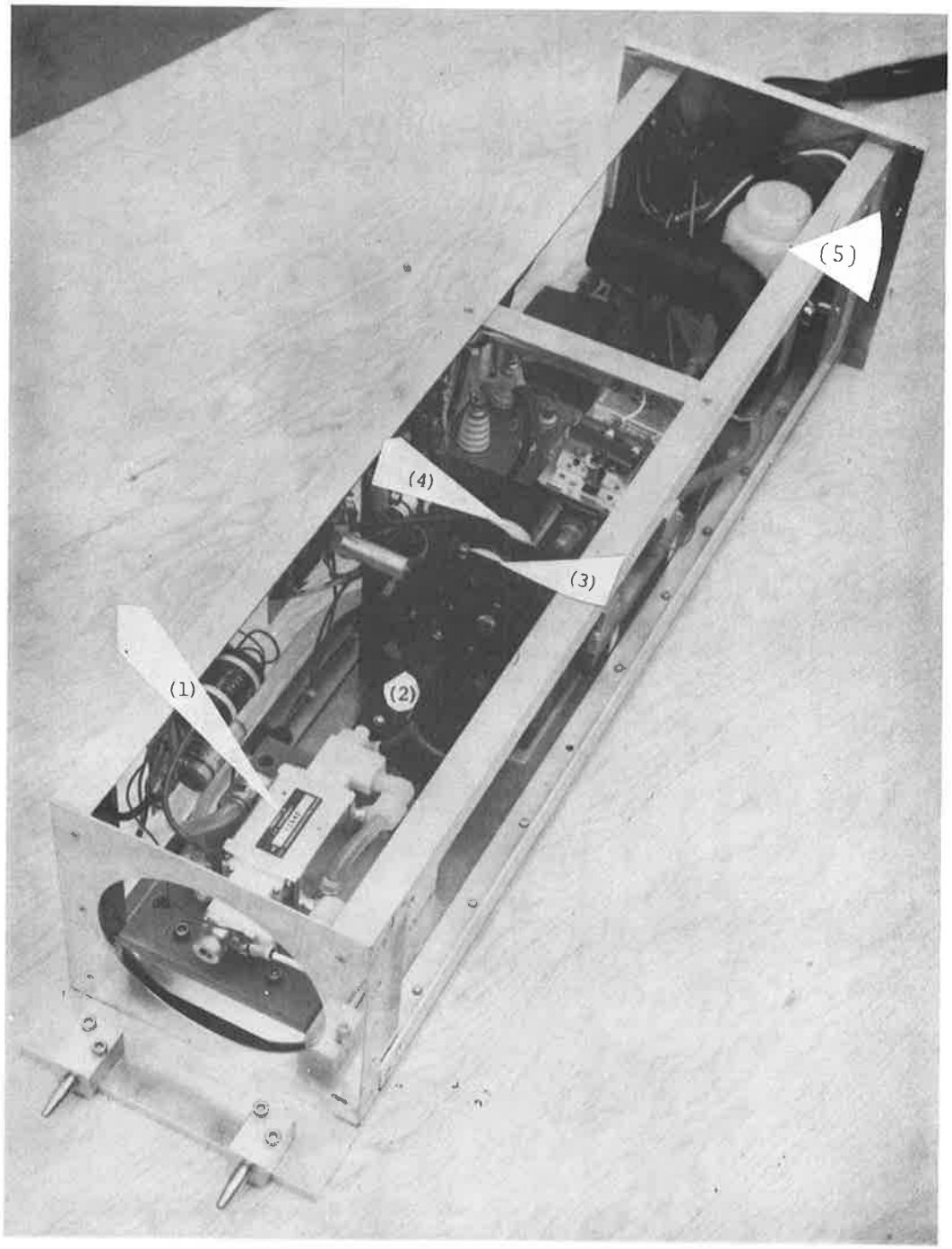


Figure 10. Module containing ruby laser. The laser components visible are: (1) cavity; (2) stacked-plate polarizer; (3) Pockel cell; (4) Rear mirror; (5) Cooling water reservoir, pump and heat exchanger fan

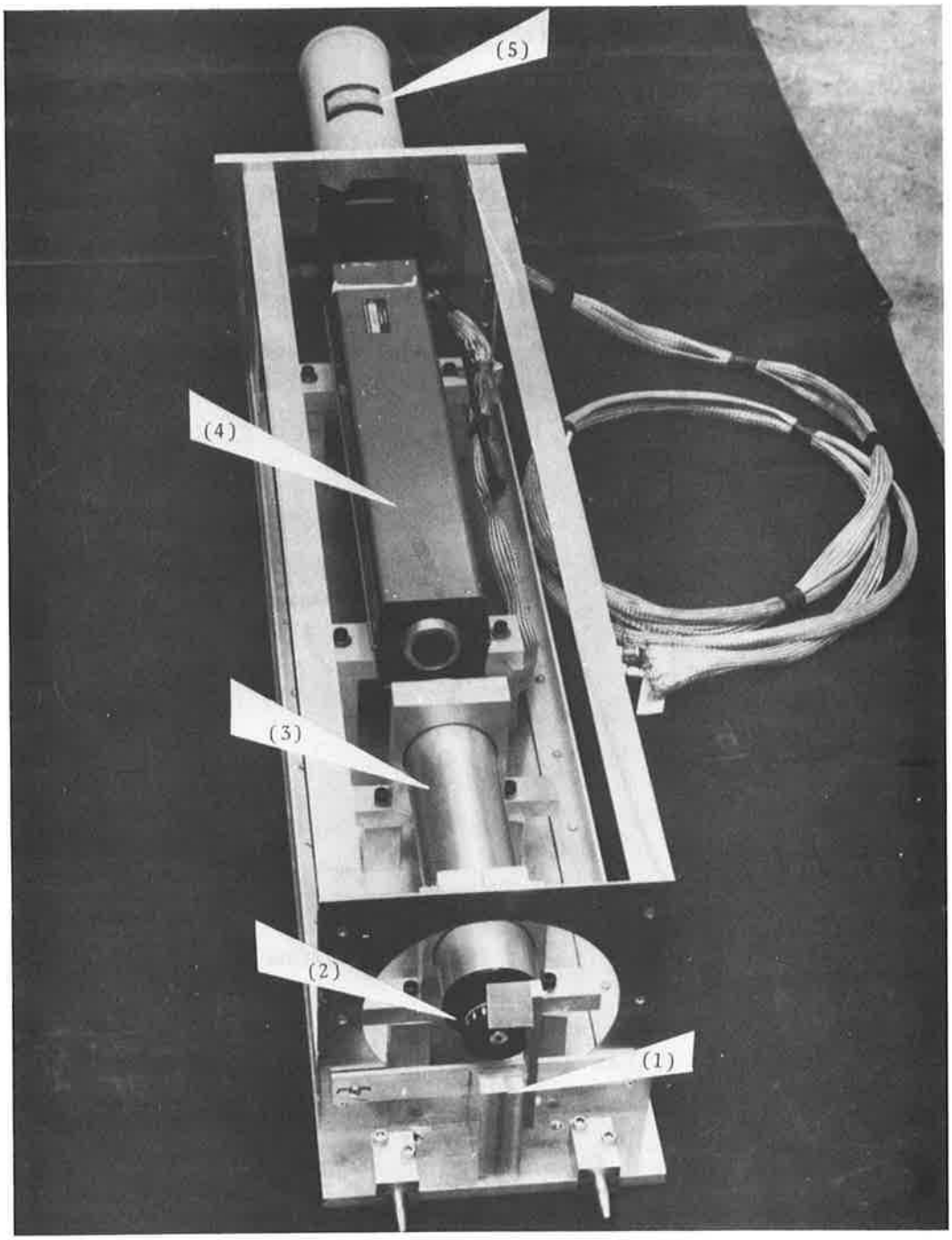


Figure 11. Helium-neon laser and modulator components: (1) reference beam splitter; (2) polarizer; (3) modulator; (4) laser; (5) reference PMT housing

provides a moderate peak power, high rep-rate source of radiation centered about a wavelength of 825nm ($\Delta\lambda$ = ±6nm). The laser, which is thermoelectrically temperature-controlled, can be used in a single pulse mode or pulsed with repetition rates as high as 1 kHz. The pulse width (full width at half maximum) of the system at present is approximately 100 nsec, with a peak power of 300 W. The output pulse shape, which fits a gaussian quite well, is shown in Figure 12. The laser array consists of several sub-arrays of

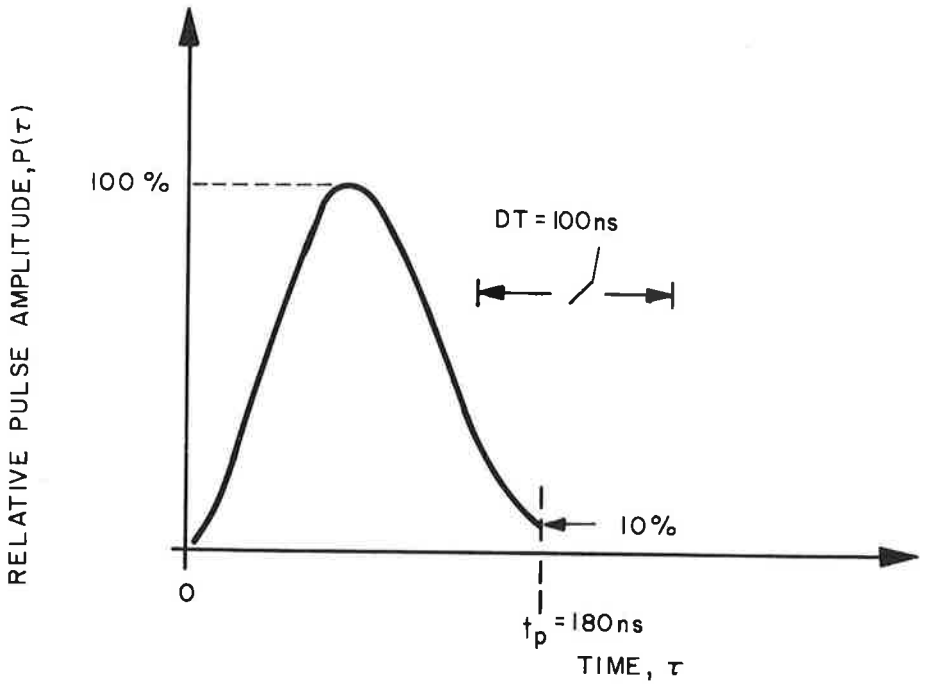


Figure 12. GaAlAs laser output pulse. Full width at half-maximum (DT)=100ns

laser diodes, mounted in a "staircase" configuration. The optical output of the array is homogenized in a quartz optical integrator. This produces an effective uniform source at the (square shaped) integrator output face (Figure 13). An f/1.5, 5" diameter output lens collimates the light. The angular divergence of the output

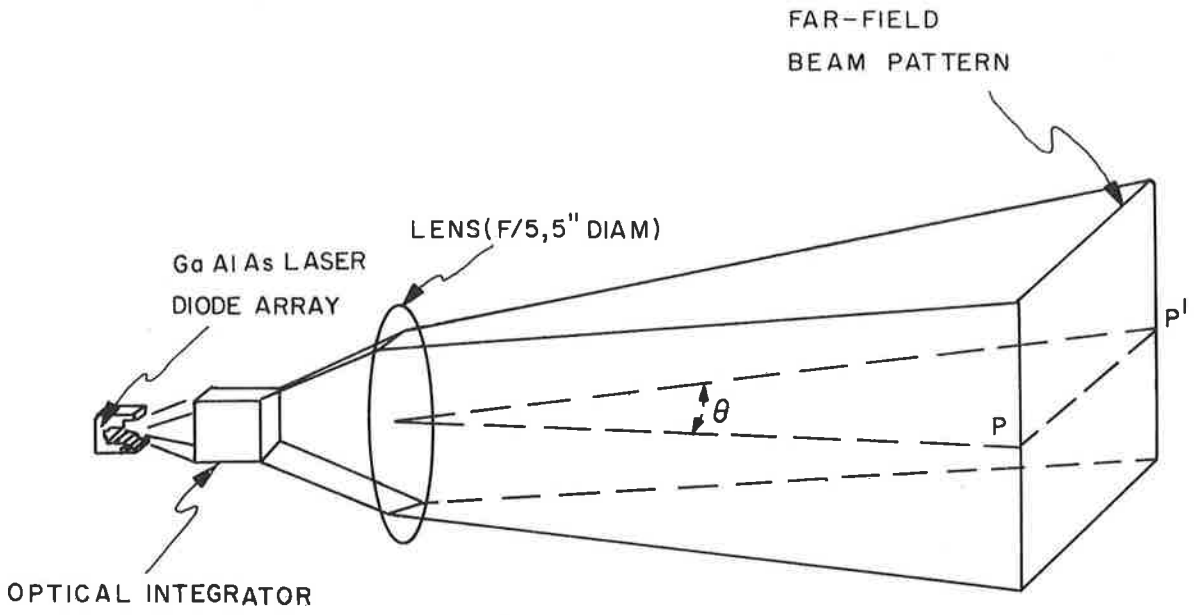


Figure 13. GaAlAs transmitter optics, drawn out of scale to show evolution of beam into a uniform square intensity distribution

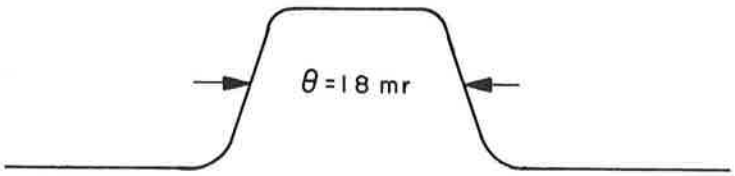


Figure 14. Scan of far-field GaAlAs beam intensity to obtain beam divergence θ shown in Fig. 13

beam is 18 mrad, measured parallel to the sides of the square (Figure 14).

The laser is operated at pulse rates above 100pps to allow signal averaging.

### 3.1.2 Optical Receiver

The optical receiver system, which is basically common to all three laser systems described here, is shown schematically in Figure 15. The objective is a 5" diameter, f/5 lens. A field stop, continuously adjustable from virtually closed to about 15mm, is positioned at the focus of the objective. A field-of-view of approximately 30 mrad, sufficient to circumscribe the (square) laser far field pattern, is used for the GaAlAs system. A narrow band filter (820nm, $\Delta\lambda$ = 15nm, peak transmission = 70%) is used and, in addition, any or all of three separate neutral density filters (Optics Technology, Inc.) can be introduced by means of a remote mechanical linkage. The light passing through the filters is first collimated by lines L1 (Figure 15) so that it enters normal to the narrow band filters. Lens L2 then images the objective onto a small diffusing disk which spreads the light uniformly over the photocathode.

The photomultipliers (PMT) which have been used for the GaAlAs work are an EMI-9558 (S-20) and an RCA 31025C. The latter has a quantum efficiency at 825nm of about 2%, but the S-20 tube, though less sensitive, has more internal gain and was used with good results. The PMT is terminated with a 50 ohm load.

A non-linear bias chain for the 9558 was used, along with zener-diode voltage regulation of the first stage and capacitors

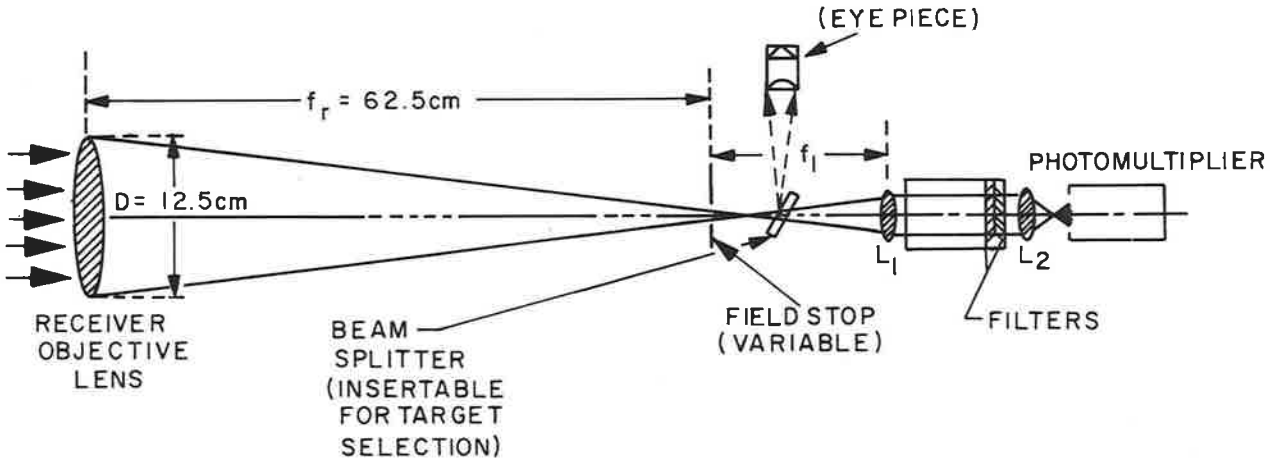


Figure 15. Schematic of lidar receiving optics

across the last stages, to ensure linearity of response under fast pulse illumination. The response was tested in the laboratory with calibrated neutral density filters and a LED source (1 μsec square pulse) and found to be linear up to anode currents of at least 10 ma (V = 1000v).

The optical axes of the GaAlAs transmitter and the receiver are separated by 10". The alignment of the two axes is accomplished at night as shown in Figure 16 utilizing the He-Ne laser, (which is described below as the source for the modulated CW technique). The helium-neon beam is made coaxial with the receiver axis by a pair of TIR prisms. The "red" beam is both highly collimated and visible, making the alignment easy to attain, using the bore sighted, off-set eyepiece. The GaAlAs laser is then used to "illuminate" a target approximately 100 feet away. By means of a hand-held image converter telescope, the square infrared beam pattern is made visible. The GaAlAs transmitter is oriented so that the center of the square falls exactly 10" from the position of the red beam, and is displaced in the proper direction (Figure 17).

The function f(R) (Section 2.3) was determined experimentally as follows: On a clear night, a large white card (approximately 2 meters square) was moved systematically along the axis of the lidar while the peak amplitude of the laser return was monitored on an oscilloscope. The large target was needed to allow readings to be made out to 50-60 meters, where the divergence of the laser caused a beam cross-section of more than 1 meter square. The power received is proportional to $R^{-2}f(R)$, and f(R) can then be obtained by multiplying by the square of the corresponding

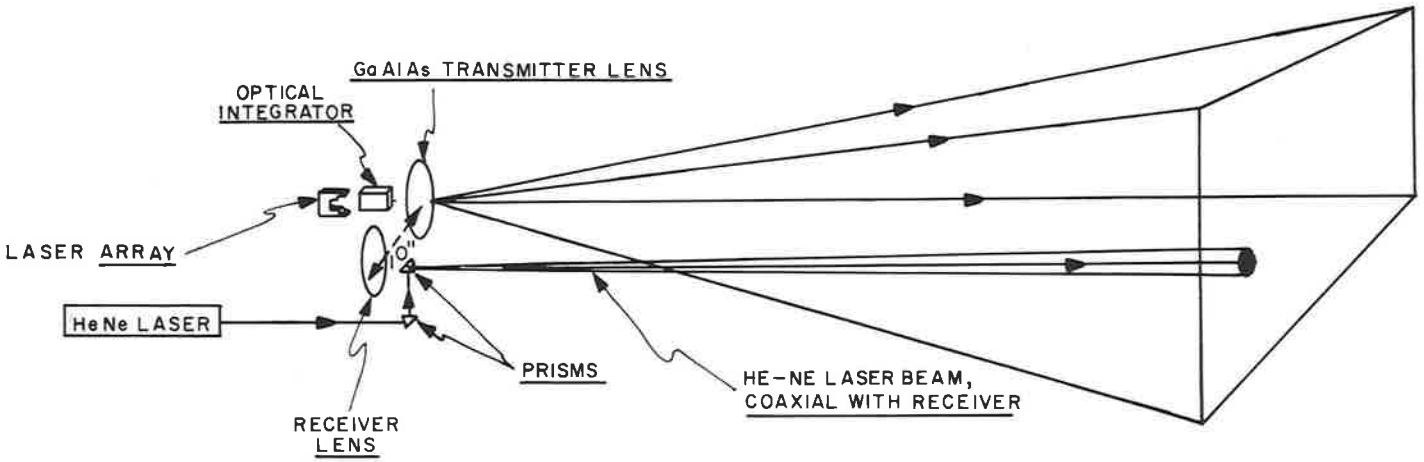


Figure 16. Alignment procedure for GaAlAs lidar, using auxiliary He-Ne laser to define receiver axis

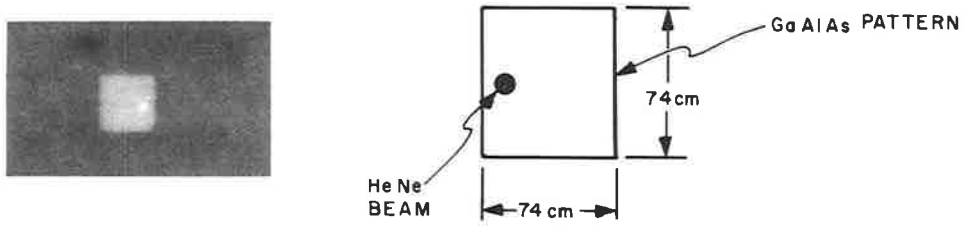


Figure 17. Photograph of GaAlAs far-field pattern, superimposed on the He-NE image, as the two beams illuminate a target 35 meters from the transmitter. Taken at night, using Polariod 413 IR-sensitive film, the picture shows the condition of alignment

range R. Figure 18 shows the measurement of the geometry function, f(R). It was found that this measurement is reasonably consistent with eq. (2-16), with $R_o \approx 12$ m.

### 3.1.3 Data Acquisition

The detected signal can be displayed directly on an oscilliscope but the signal-to-noise ratio is not adequate for accurate readings. The noise arises predominantly from intensity fluctuations in the background radiation. In addition local variations in fog density due to wind or convection effects lead to noise-like features of a different nature.

Signal averaging is used to enhance the lidar accuracy. Two somewhat different approaches have been tried. The earlier approach employed a box-car integrator (Princeton Applied Research, Model 160) which averages many consecutive return pulses, selecting for integration a narrow portion of the pulse shape by means of a scanning gate. As a given slice of the pulse is integrated (random noise being averaged to zero with an effectiveness proportional to the square root of the integration time), the resultant signal is available for driving a recorder. The time required to scan the entire lidar return pulse is determined by factors such as pulse repetition rate, gate aperture and integration time constant. With the experimental parameters imposed by resolution and accuracy, the minimum sweep time was 1-2 minutes.

The boxcar integrator was used in a series of tests made in coastal fog at Lubec, Maine during July of 1972. These tests served as precursors to the Richmond field tests conducted in 1973. Analyses of the lidar signals obtained with this "integrate-

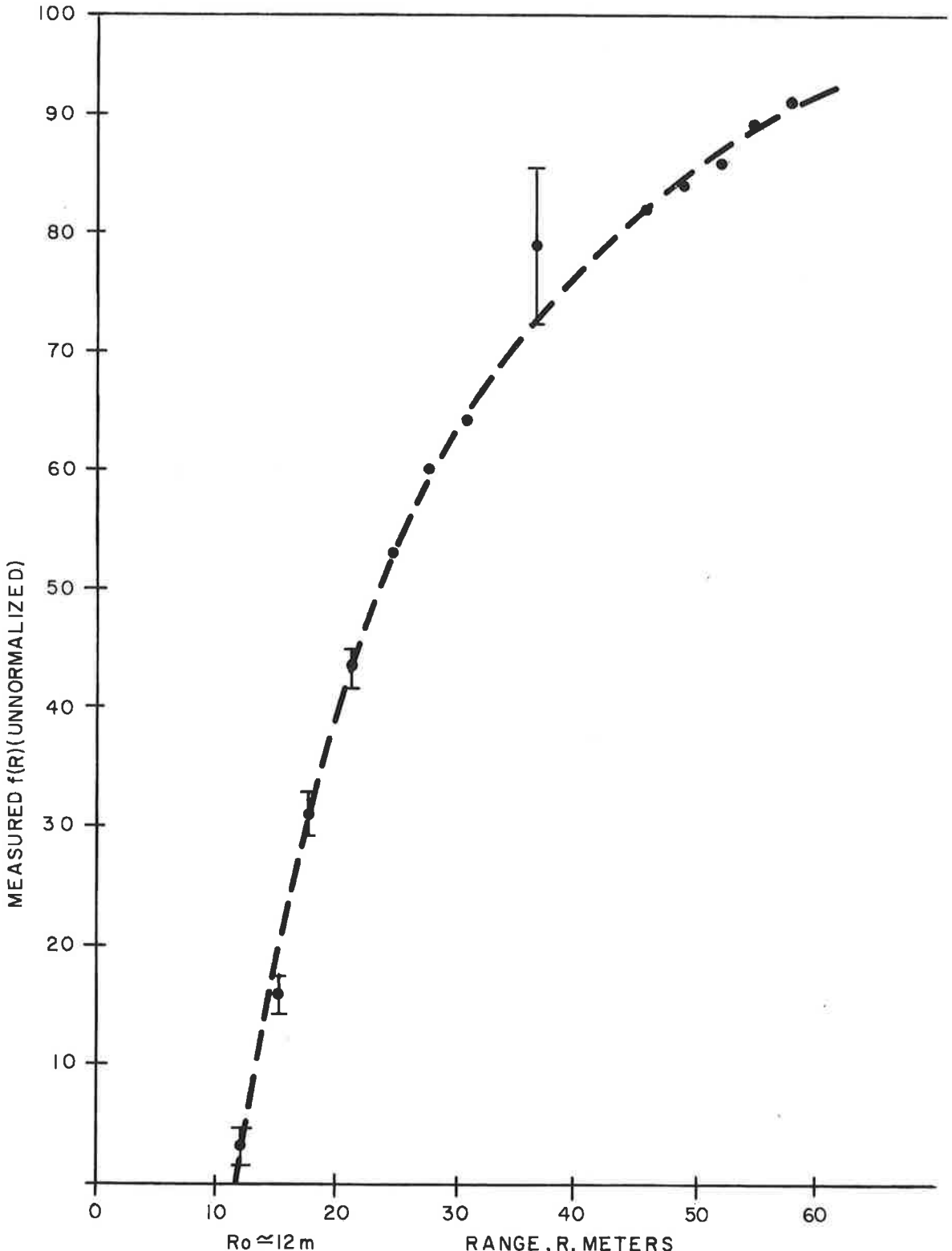

Figure 18. Measurement of geometry function f(R) for GaAlAs system

and-scan" method showed reasonable agreement with visibilities observed by eye and those deduced from lidar. (These early tests were analyzed without the aid of the computer program which takes account of laser pulse shape.)

The boxcar technique is especially well-suited to situations where the signal is repetitive and reproducible. This is clearly not the case for signals backscattered from fog which can be quite variable, even over periods of a few seconds.

Partly because of this, and partly to facilitate the development of an automatic digital acquisition and reduction system, a second approach was implemented. In this method, the entire return signal (including noise) is acquired for each return pulse. Averaging is then done over many such acquisitions. Although in uniform and/or static fog formations the two methods will give the same results, for certain time-varying fog conditions the latter technique is probably more reliable. In the present work, analog averaging is used and a discussion of the experimental arrangement follows.

The signal from the PMT, after amplification by a factor of 10, is introduced to a Biomation Model 8100 Transient Recorder (TR) which digitally records the amplitude in 2000 consecutive 8-bit channels, each of which is 10 nsec wide. This will be useful for automatic processing when a computer interface is added. However, we did not perform the field tests in an automatic mode and, since the TR cannot store more than one pulse at a time, an auxilliary method for averaging pulses was necessary.

The averaging of successive pulses is accomplished by scanning the memory of the TR after each pulse, and reading the

(analog) amplitude into a waveform eductor (WE), (Figure 19). The TR output scan rate is fixed at 1 kHz and optimum resolution is obtained by using a sweep duration of 100 μsec for the waveform eductor. Since the sweep of the WE is synchronized to the TR sweep, only the first 10% of the millisecond sweep period of the TR is transfered to the waveform eductor. This corresponds to the first 10% of the 20 μsec TR base, or 2 μsec., and is more than adequate to encompass completely the time range over which the return signal occurs.

The output of the waveform eductor is taken from 100 sequentially-scanned capacitors, yielding 100 corresponding voltages which can be smoothed by a filter providing a smoothing bandwidth consistent with resolution of 1/2% of the time base (1/2% x 2 μsec. = 10 nsec.). It is important to realize that the output of the WE represents a time average over a period of about one minute. This is due to a product of time constant and duty cycle effects. Although preferable to the boxcar averaging method, the significance of an average over such a long time is not clear, and the ruby lidar (see below), which allows single-pulse analysis, was included to give a basis for evaluating this significance.

The output pulse shape representing P(t) is available from the WE either as an oscillogram or, via a Hewlett-Packard Scanning Oscilloscope, as an X-Y recorder trace. The latter provides a hard copy of the function displayed on the oscilloscope, and with an expanded format.

The signal-to-noise improvement ratio (SNIR) expected at the eductor output (assuming the noise is random) depends on the number n of traces averaged. The value of n is related to the

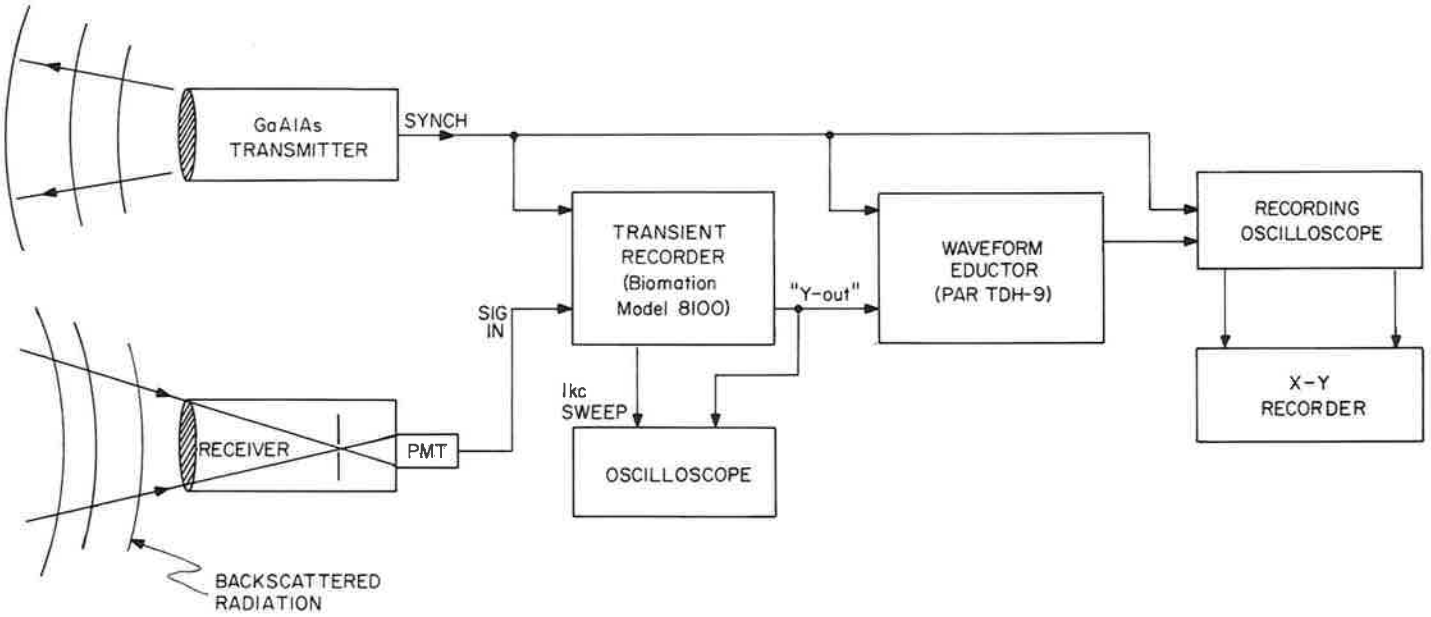


Figure 19. Signal processing system (GaAlAs lidar)

eductor sweep duration ($t_{SD}$) and the characteristic time constant $t_c$ of the eductor. It can readily be shown that $n = 5\ (t_c/t_{SD})$. Then, $SNIR = \sqrt{n} = 2.2\ \sqrt{t_c/t_{SD}}$. Using $t_c$ = 1 sec, $t_{SD}$ = 100 μsec, we find SNIR = 220. As mentioned above, however, the duty factor was 10%, resulting in a value of n one-tenth as large and SNIR=70.

## 3.2 RUBY LIDAR

### 3.2.1 Ruby Laser Source

The ruby laser, operating at a wavelength of 694.3nm, is Q-switched by a Pockel cell and is capable of peak power outputs of 50 Mw in 20 nsec pulses. The beam divergence is 5 mrad (full angle). Built to specification by Raytheon (Advanced Laser Development Center, Waltham, MA), the system uses a 3" x 1/4" rod and is water-cooled, allowing pulse rates up to 6 ppm. The layout of laser components is shown in Figure 10.

Figure 20 shows a schematic of the arrangement of the ruby lidar system. The optical axes of the laser and the receiver are made coincident by a pair of TIR prisms.

### 3.2.2 Optical Receiver

The same receiver is used for both the ruby and GaAlAs lidar, although the field stop and optical filters are different for each. For the ruby case, a field-of-view of approximately 10 mrad is used.

The backscattered signature is stored in the transient recorder after each shot, and is simultaneously presented on the recording oscilloscope. The latter permits selection of data for hard-copy recording on an x-y recorder.

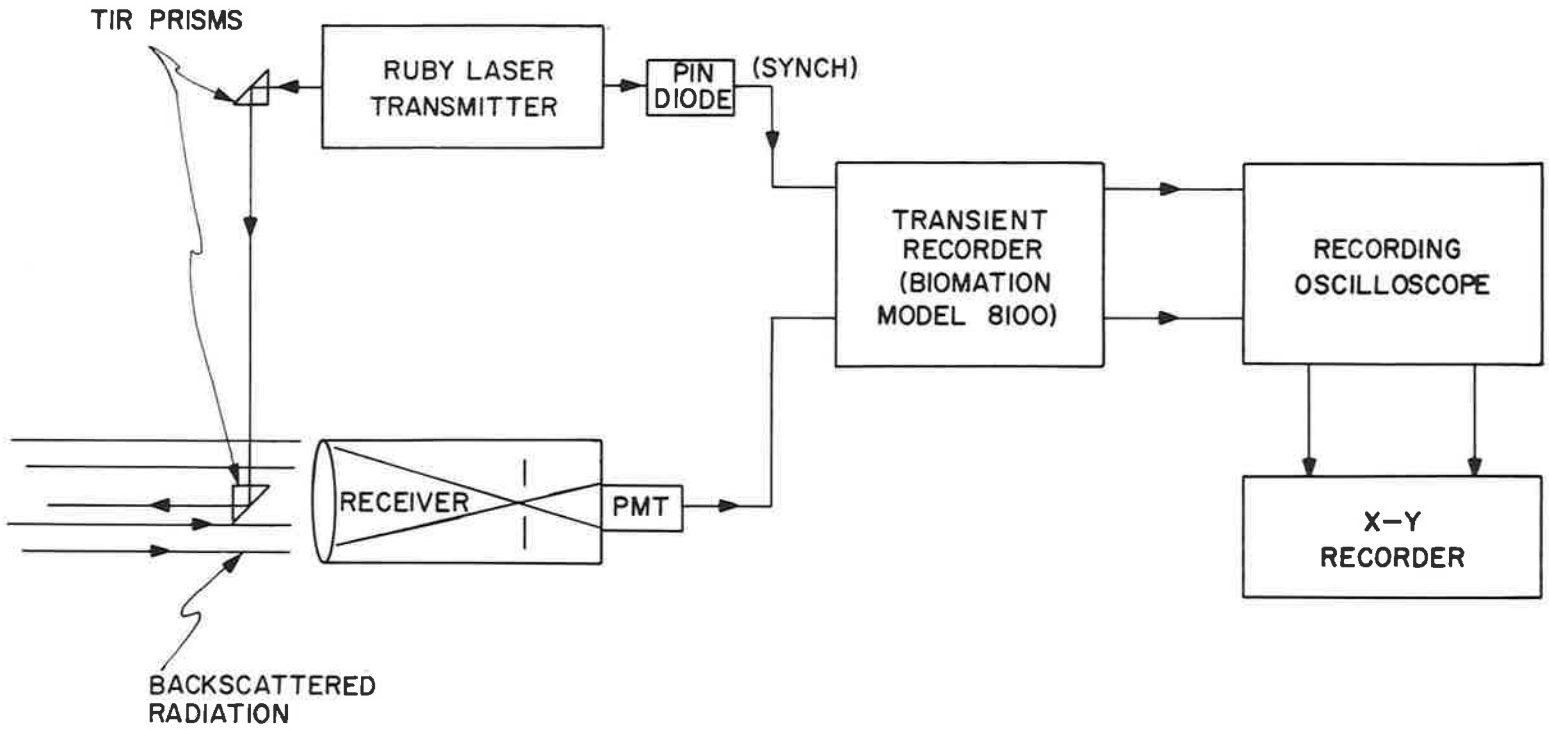


Figure 20. Signal processing system (ruby lidar)

The geometry function f(R) was measured by simulating the ruby beam with a coaxially-mounted helium-neon laser, adjusting the output beam size and divergence to match those of the ruby laser. The results of the measurements and the fit of the data to $[\tanh (KR)]^3$, are shown in Figure 21.

## 3.3 MODULATED CW LIDAR

### 3.3.1 Helium-Neon Laser Source

The CW optical source for the transmitter is a helium-neon laser ($\lambda$ = 632.8nm) having approximately 5 mw output power. The beam is passed through a Glan polarizer and then through an electro-optic modulator, in such a manner that the intensity passing the analyzing polarizer (Figure 22) varies sinusoidally at frequency f (where f ranges from 1 to 10 MHz). The direction of the modulated laser beam is then made coincident with the receiver optical axis by the pair of beam-directing 45° prisms. Part of the modulated output beam is directed by a beam splitter onto a "reference" PMT ($PM_1$). The average transmitted power is about 2 mw, and the extent of intensity modulation is approximately 30%.

### 3.3.2 Optical Receiver

The same receiver is used as previously discussed, with a field-of-view of 3 mrad and a narrow band filter of 3nm bandwidth.

The signal PMT as well as the reference PMT are both EMI 9558 photomultipliers.

### 3.3.3 Signal Processing for the Modulated CW Lidar

The signal from $PM_2$, corresponding to the photocurrent due to backscatter, and the reference from $PM_1$, are sent to a vector

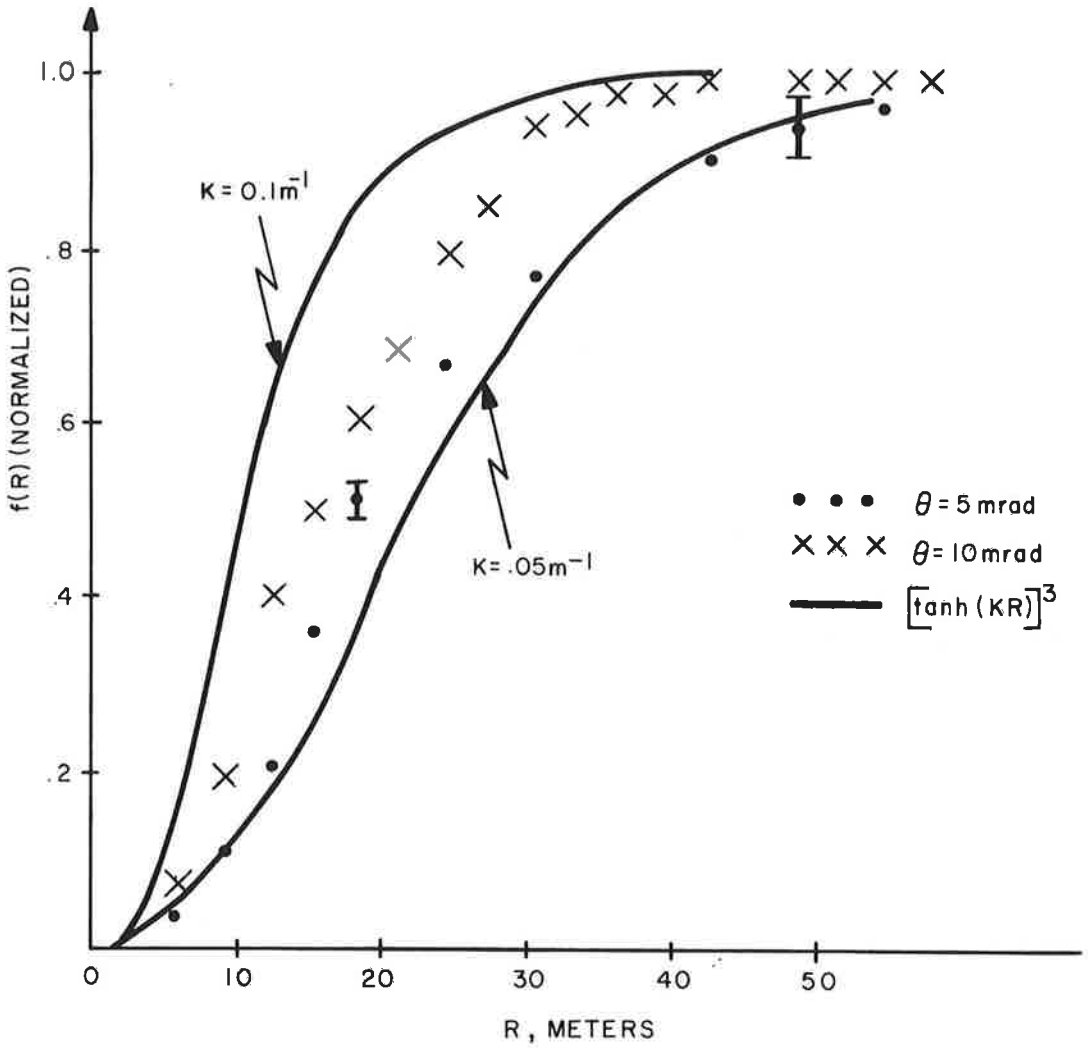


Figure 21. Measurement of geometrical function f(R) for coaxial lidar system. Dashed curves represent $[\tanh(KR)]^3$ for K=0.1 and $0.05m^{-1}$. Measured curves are for data obtained with two receiver fields-of-view. The ruby beam was simulated both in divergence (5mrad) and size by a helium-neon laser

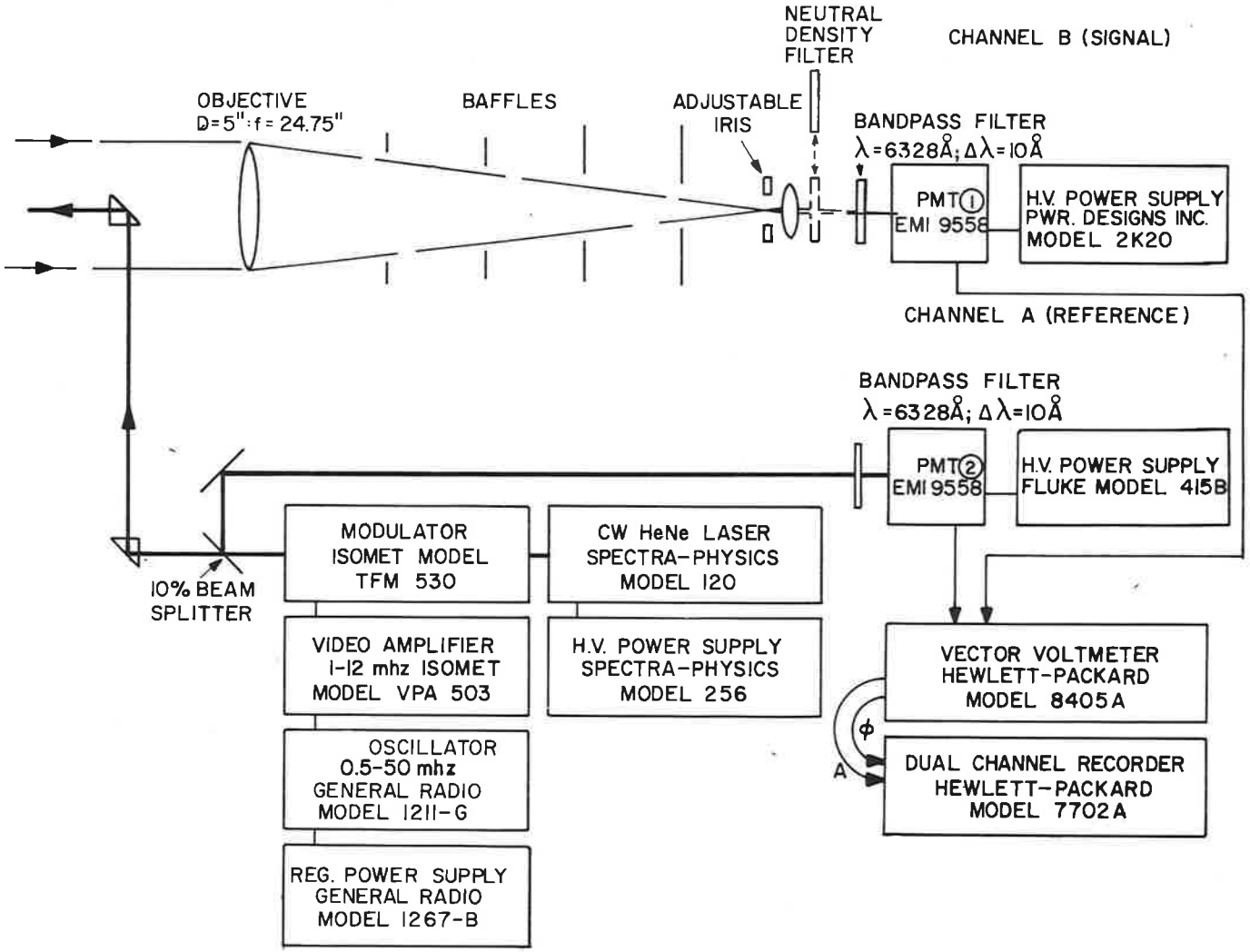


Figure 22. Block diagram of modulated CW lidar: Modulation and detection scheme

voltmeter (Hewlett-Packard 8405A). This instrument measures the amplitude and phase of an input signal when a reference phase ($PM_1$) is available. The noise equivalent input of the meter is 10 μvolts. The measured amplitude and the phase of the signal are fed to a dual channel recorder, and changes in either can be observed as the modulation frequency f is varied.

In practice, the relative phase is zeroed by directly scattering modulated light from the transmitter into the receiver, using a target placed essentially at zero distance. When this work was first begun, a PIN photodiode was used as the reference detector. It was subsequently discovered that the relative phase could be zeroed at only one modulation frequency (for R = 0) and in general was a linear function of frequency. This frequency - dependent phase shift was found to arise from two causes. Most of the contribution came from photoelectron transit times in the PMT. A smaller shift came from the reference-signal residual optical path inequity.

By replacing the diode detector with a second PMT (similar in structure to the first PMT) it was possible to remove <u>both</u> these effects in a novel manner. If we represent by $\Phi_s(R)$ the phase of the photo current generated at the anode of the signal PMT, due to light reflected from range R, and by $\Phi_R$, the corresponding phase of the reference PMT, then

$$\Phi_s(R) = \phi_o + \omega\left(\frac{2R}{c}\right) + \omega t_2$$

and

$$\Phi_R = \phi_o + \omega\left(\frac{\Delta L}{c}\right) + \omega t_1 \quad .$$

The quantity $\Delta L$ represents the residual optical path difference of the two channels and $t_1$, $t_2$ are the electron transit times for the reference and signal PMT's, respectively. The measured relative phase, for R = 0, is given by

$$\Delta\Phi(o) = \Phi_s(o) - \Phi_R = \omega\left(t_2 - t_1 - \frac{\Delta L}{c}\right) \quad .$$

This demonstrates the linear dependence of $\Delta\Phi(o)$ on $\omega$. The transit time is a function of PMT bias voltage. For the EMI 9558, this dependence is approximately $t = AV^{-1/2}$ where $A \simeq 2.5 \times 10^{-6}$ sec-volt$^{1/2}$. Thus by proper adjustment of $V_1$, $V_2$, the quantity $(t_2 - t_1 - \frac{\Delta L}{c})$ can be made zero. Experimentation showed that a suitable choice was $V_1$ = 820V, $V_2$ = 1000V. For these values of PMT bias, there was essentially no relative phase shift observed (for R = 0) as the frequency was varied from 2-8 MHz. Calculation gives $t_1(820V) \simeq 90$ ms and $t_2(1000V) = 82$ ns and thus a residual optical path difference of about 8 ns (=8ft.), which is roughly what is expected due to relative positions of reference and signal PMTs in the lidar apparatus.

# 4. FIELD TESTS OF TSC LIDAR INSTRUMENTATION

## 4.1 INTRODUCTION

In July, 1972 and again during the month of May, 1973, the TSC lidar system was tested in the field. The first of these tests took place at West Quoddy Head lighthouse near Lubec, ME. The ruby laser had not yet been acquired. Also, as has been mentioned earlier, the boxcar integrator approach was taken to data gathering. Although the data gathered at Lubec with the GaAlAs system were quantitatively encouraging, the main goal of these tests was the characterization of the signal and background levels and the effects of environment on optical and electronic components.

The second field test was conducted at the Richmond Field Station Fog Chamber, Richmond, CA. This site was chosen for several reasons. The potential for data-gathering in the chamber is much greater than under naturally-occurring conditions since fog can be produced at will. In addition, it was expected that conditions in such a chamber would be relatively homogenous, stable and reproducible, in contrast to common experience with natural fog. Tests conducted in the chamber would then allow lidar performance to be analyzed without the disturbing ambiguities which usually accompany unstable and inhomogenous fog. Unfortunately the chamber was not as free of these kinds of problems as had been expected.

Both field tests will be discussed in the following sections.

## 4.2 FIELD TESTS AT LUBEC, ME

### 4.2.1 General Description

As a natural site at which to test the TSC lidar apparatus, the coast of Maine offered at least as high a frequency of heavy fog as any other site on the east coast. Through the cooperation of the Southwest Harbor Group of the U.S. Coast Guard, the lighthouse grounds at West Quoddy Head, Lubec, ME were made available for TSC lidar experiments. For three weeks during July 1972, tests were conducted using the GaAlAs and CW helium-neon lidars. (The ruby laser had not been delivered from the manufacturer and was therefore not included in these early tests.) The equipment was transported in a Cortez van (Figures 23, 24) with relay racks installed in the van to carry the auxilliary electronics. The lidar frame (with the tripod base removed) was supported in use by an adjustable platform which allowed the apparatus to be pointed out of the van window.

The orientation of the lidar was limited to the range of directions accessible from this window. In general, the aiming direction was seaward, at an elevation angle of approximately 10-15 degrees. The first 30-50 feet of beam path was over land, and the remaining length was over water. The elevation of the land was approximately 20-30 feet above sea level. In the same direction, two distinct rock formations, at distances of 510 and 1300 ft, provided reference targets for estimating visibility (Figure 25). In addition to these rocks, some large land obstacles which stood out against the sky and were at convenient intermediate distances (phone poles, trees) were used as targets. Particularly

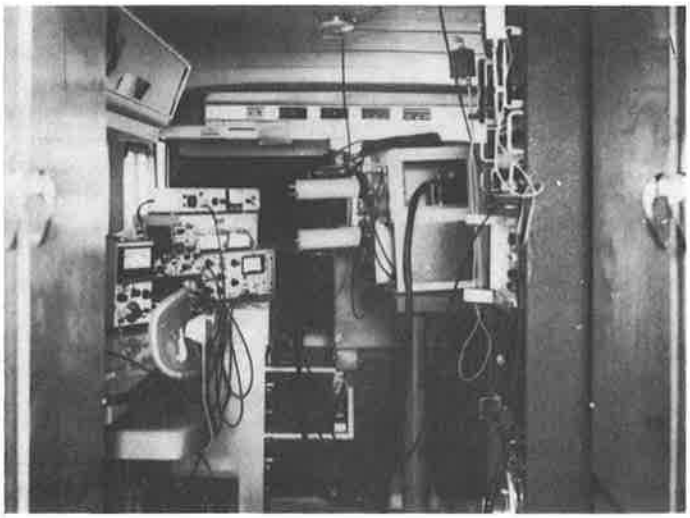

Figure 23. View of lidar and associated electronics as installed inside mobile van at Lubec, Maine


Figure 24. Cortez van equipped for lidar field test at Lubec. Transmitter and receiver optics can be seen through the side window

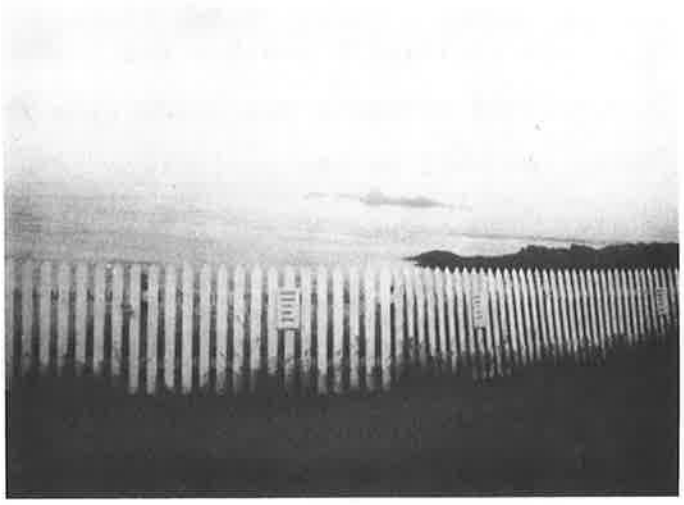

a)

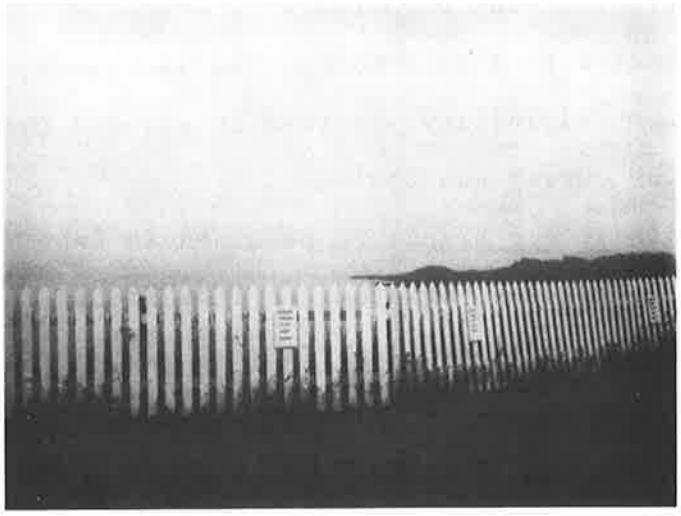

b)

Figure 25. Rock formations off West Quoddy Head (Lubec) used as visibility references. Distances of formations are approximately 510 and 1300 feet. a) weak fog. b) heavier fog, with estimated visibility ~ 900 - 1000 feet

when the fog was "socked in", these points gave reasonably repeatable (though not necessarily accurate) estimates of extinction.

The incidence of low visibility weather was high during the stay in Lubec. This allowed adequate operating time for "debugging", alignment, etc., as well as the collection of a large number of lidar signatures from fog.

### 4.2.2 GaAlAs Lidar Results (Lubec)

Generally, the fog moved in from the sea at about "2 o'clock" with reference to the pointing direction of the lidar. Moving rapidly, it soon covered the entire panorama and usually appeared to be uniform. Once established, the fog generally remained for many hours (often days) at a time, with the average visibility fluctuating from perhaps 500 ft. at the minimum to about 2000-2500 ft. These fluctuations occurred with characteristic times ranging from 5 minutes to a half-hour. Qualitatively, the relationship between visibility observed by eye and the shape of corresponding lidar curves was obvious.

Only one GaAlAs lidar signature obtained in Lubec has been reproduced here (Figure 26), in order to indicate the quality of the data. Figure 26a shows the experimental signal from the box-car recorder (solid curve). The ratio method was used to deduce $\sigma(R_1,R_2)$. The relative S-function [$=\ln(PR^2/f(R))$] deduced from this signal is plotted in Figure 26b. The slope method was used, between $R_A$ and $R_B$, to determine $\bar{\sigma}_{AB}$. The visibility was estimated by eye to be 150 meters, which, by Koschmieder's relation (eq. 2-9) gives an extinction coefficient of $\sigma = .026m^{-1}$. The values

found for the trace of Figure 26 were: $\sigma(\text{ratio}) = .021\text{m}^{-1}$, $\sigma(\text{slope}) = .019\text{m}^{-1}$. Accepted at face value, these results indicate good inter-agreement. Though several other runs gave comparable consistency, there were also some which showed poor agreement.

Several factors suggest that the agreement is probably not as significant as Figure 26 would indicate. For one thing, the "short pulse" assumption was used in analyzing these data, even though the laser pulse was greater than 100 ns. It was found that when the finite source width was taken into account the consistency was gone.

Furthermore, in laboratory tests subsequent to the Lubec work, it was found that the PMT response became non-linear for peak anode currents greater than 100-200 μA, whereas signal currents as large as 1mA were included in the lidar data. (The circuitry has since been altered bypassing the last few dynode resistors with capacitors, with the result that pulse amplitude linearity is maintained with currents as large as 5-10 mA. The altered PMT circuitry was used for the Richmond work.)

Finally it is clear from the exhibited lidar trace that variability is present. This can cause large variations in the extracted value of the extinction coefficient. In particular, the choice of $R_1$, $R_2$ and $R_A$,$R_B$ is somewhat arbitrary. For example, had the choice $R_A = 75\text{m}$, $R_B = 100\text{m}$ been made, the "least squares" slope would have yielded a value for $\bar{\sigma}_{AB}$ approximately 50% larger than given above. Likewise, the choice $R_A = 50\text{m}$, $R_B = 75\text{m}$ yields $\bar{\sigma}_{AB}$ smaller by the same amount. More experience is required to minimize these effects as they pertain to operational uncertainties.

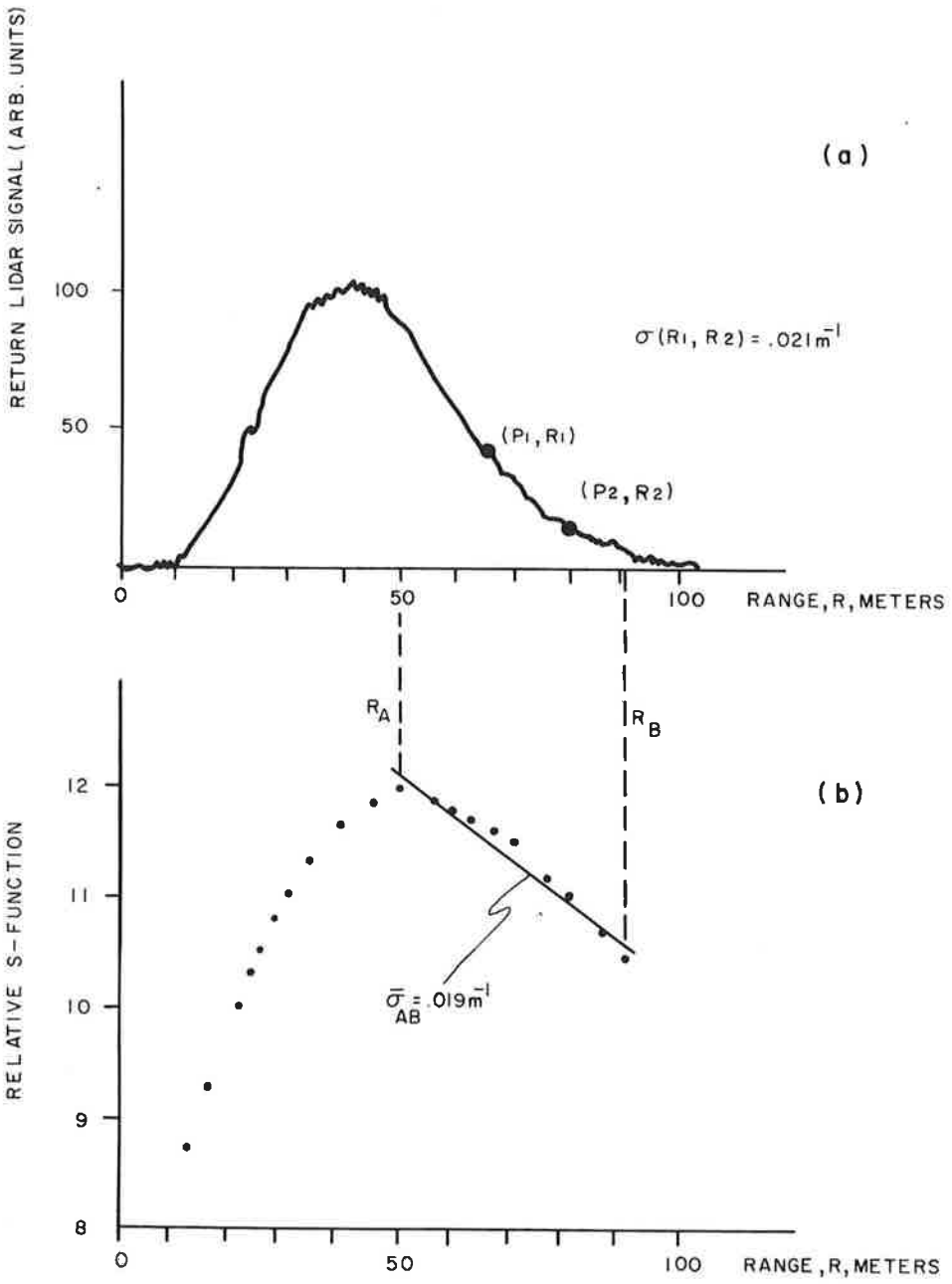


Figure 26. Data from GaAlAs lidar, Lubec, ME. Estimated visibility =150 Meters. ($\sigma$=3.9/150 = .026m$^{-1}$). a) Boxcar integrator output; Time constant = 1 sec., Scan time = 120 sec. Lidar prf=144 pps. Ratio method was used to deduce $\sigma(R_1,R_2)$. b) Relative S-function (=ln($PR^2$/f(R)) deduced from experimental trace (a). Slope method used to determine $\bar{\sigma}_{AB}$

It must be recognized that the S-function analysis has been based on an idealized (i.e., short pulse) model of the lidar signal. (The same is true of the S-function analysis of the Richmond data below.) Hence slope variations such as occur in Fig 26b may arise from the non-ideal (i.e., broad) pulse shape. In support of this possibility is the fact that finite source pulse effects contribute less at larger values of range. The application of the ideal lidar equation to the S-function tends in general to underestimate the slope (and hence $\sigma$). Therefore, at larger values of R, the slope should increase (assuming uniform fog conditions), and this is the behavior usually seen.

### 4.2.3 Modulated CW Lidar Results (Lubec)

In spite of numerous attempts to observe a visibility-dependent signal with the CW lidar, none was found. The attempts were made at night in order to eliminate background noise. Often, as the frequency of the rf was varied from 1 MHz to above 8 MHz, a sharp phase variation (as measured by the output of the vector voltmeter) was observed near certain frequencies. However, in every case, the phase "transition" was found to be unrelated to backscattered radiation and appeared to be due to spurious rf pickup. Discussion is deferred to section 4.3.4.3, below.

## 4.3 FIELD TESTS AT THE RICHMOND FOG CHAMBER

During a 3 week period in May, 1973, the TSC lidar apparatus was tested in the Fog Chamber at Richmond, CA. A considerable amount of data was collected under reasonably controlled conditions. The essentially unlimited availability of low visibility conditions made it possible to verify alignments, optimize

signal conditions, ascertain background and zero levels and calibrate read-out devices, all within an experimental framework of a reproducible environment.

At this stage of the lidar development it was important to test the system for internal consistency with regard to the analysis of the backscatter signature. This was particularly true because of the need to take account of the outgoing laser pulse shape in the analysis. To assess the accuracy of the analytical method used, it was desirable to keep unknown or unpredictable factors to a minimum. The fog at the station was found to be more inhomogenous and variable than had been anticipated, adding significant difficulty to the analysis. Nevertheless the data show good consistency and support the validity of the lidar method of measuring extinction coefficients.

### 4.3.1 Description of the Fog Chamber

The fog chamber at Richmond Field Station is a wood frame structure 1000 feet long and 30 feet wide. The sides of the building are covered with corrugated sheet steel panels, on the bottom half, and with translucent fiberglass panels for the upper half. The roof also consists of translucent fiberglass.[11] The ceiling, which is approximately 27 feet high at the "near" end of the building (where lidar is installed), gradually decreases in height to ten feet halfway down the building (~500 ft.).

The fog is produced by allowing a combination of compressed air and water to be sprayed out through a number of atomizing nozzles. These nozzles are distributed along the sides of the chamber. The spray is turned on and off by controlling the flow

of water to each nozzle with a solenoid valve. Compressed air (~60 psi), provided by diesel-driven rotary compressors, is run continuously. The fog particle size depends on the air-to-water pressure ratio. According to reference 11, the usual setting is for 10-20 μ particles.

The fog generating system is divided into 22 sections (or "bins") for control purposes, each separately controlled by an automatic cycling device. The cycling is based on feedback information supplied by twenty-two separate short base line IR transmissometers.

The appearance of the fog as it evolves in the chamber is seen from the sequence shown in Figure 27. The photographs were taken looking along the lidar direction. A series of circular black disk targets can be seen in the distance in Figures 27a and b. Also, fog striations to be discussed below are shown clearly in Figure 27c.

The fog conditions were set by personnel in charge of the test facility. The chamber was first filled to a high density of fog and then allowed to settle to a specified level of transmission. The controls were adjusted to give the same transmissions in each bin. Each bin, approximately 54 feet long, is fed by 4 or 6 sets of nozzles, each set consisting of a pair (or trio) of nozzles placed vertically at about four, ten (and twenty) feet from the ground. The sets are placed in pairs on opposite sides of the building.

The transmission of each bin is monitored by a transmissometer placed so that it samples a path 63 feet long, diagonally across the bin and at a height of two to four feet above the

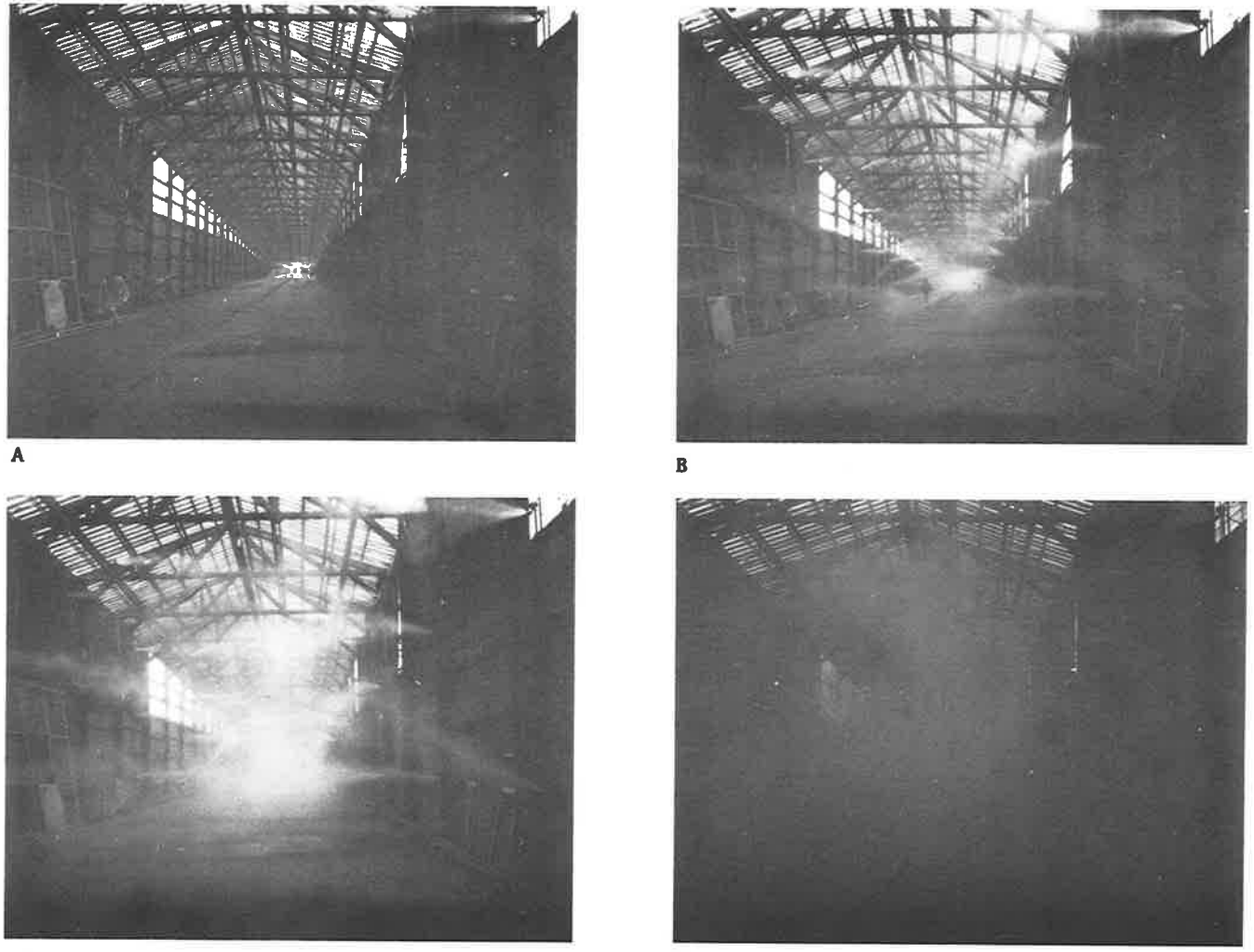


Figure 27. Evolution of fog in Richmond chamber, shown in successively denser conditions. Entire sequence spans about 1 minute

ground. The transmissometers use an incandescent source, chopped at 1 KHz. An optical filter in front of the receiver, in association with a Si photo detector, restricts the effective source spectrum to a band from approximately 800 to 1000 nm.

It is important to realize that such a method necessarily produces a fog which is non-uniform spatially at any given moment. Monitoring of individual transmissometers showed variations of about ±10% in the value of transmission read at different instants over the nozzle pulsing cycle. Averaged over time intervals ranging from about 3 to 10 seconds, however, successive transmissometers readings tended to the same value, within a few percent.

In addition to the above time-dependence of the transmission through any bin, there was a more or less constant structure to the fog distribution arising from the separation between sets of nozzles. This led to a longitudinal "segmentation" of the chamber in which the fog was denser in the regions where a transverse pair of nozzle sets existed, and less dense in the intermediate region. This non-uniformity was apparent as one walked the length of the chamber while fog was being generated. Furthermore, on cessation of the fog conditions, the floor of the chamber regularly showed alternating wet and dry patches which corresponded to the same cause. (These patches are shown schematically, approximately to scale, in Figure 28.) Any fog in the regions between adjacent pairs of nozzle sets arises from diffusion of the mist from the regions in which the water is initially introduced. As Figure 28 clearly indicates, the longitudinal diffusion rate was not comparable to the vertical settling rate.

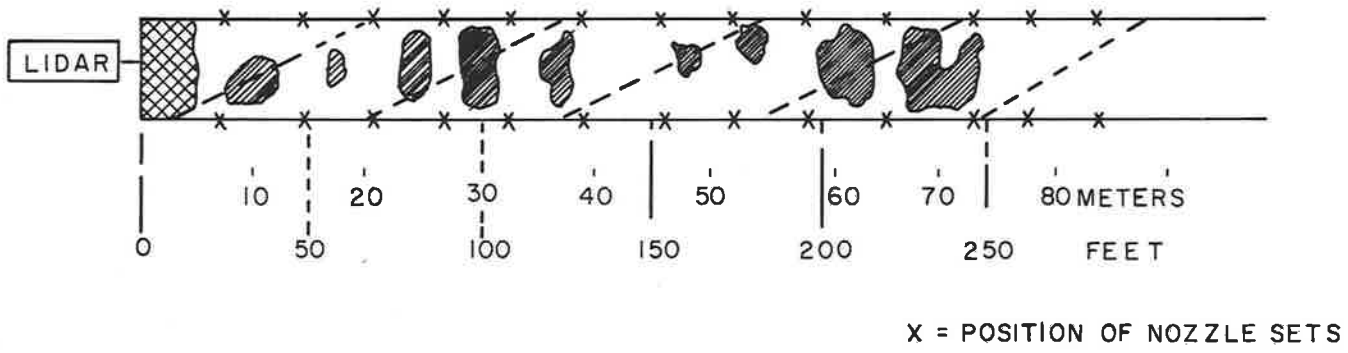


Figure 28. Plan view of Richmond fog chamber, showing dry regions (shaded) after fog is turned off. Dashed lines show transmissometer lines of sight

Both of the above effects represent limitations to the interpretation of the experiment, particularly with regard to the ruby data.

### 4.3.2 Measurement of the Extinction Coefficient

It was originally intended to use contrast targets to correlate lidar measurements with visibility in the chamber. Large black disks, subtending at least 1/4°, were positioned at 100 foot intervals starting at a range of 250 feet. However, it was soon found that these targets were unreliable in estimating visual range, apparently due to the lack of a suitable "horizon" against which the targets could be viewed. The fog chamber narrows down toward the far end, with the floor rising slightly and the ceiling decending so that the height of the chamber goes from over 25 feet at the near end to less than ten at the distant end. As a result the targets are viewed against a non-uniform background (consisting of the receding asphalt floor, grey walls etc). Furthermore, since the targets had to be separated sufficiently to be resolvable, each target was seen against a different background. (See Figure 27a.)

These factors caused the targets to be more difficult to detect, under any given visibility, than would be true if they were observed against a uniform horizon sky (with the intrinsic contrast $C_o = 1$). Extinction coefficients based on the target-derived visual range were usually much larger than derived from the averaged transmissometer readings (see below). Supporting the conclusion that the poor target background caused the visibility

to be underestimated is the fact that rafters on the top and sides of the chamber, outlined against the bright sky, were clearly seen even when their distance was as much as twice the range of the farthest visible target.

As a result, the average of the transmissometer readings ($\bar{T}$) monitored over the part of the chamber used (about 450 feet, or 8 bins) was chosen as a reference basis for the lidar. This average was obtained electronically and displayed on a digital voltmeter. The average extinction coefficient $\bar{\sigma}$ is then obtained as $\bar{\sigma}(\bar{T}) = - \frac{\ln \bar{T}}{b}$ , where b = baseline (19.2m). This relationship is plotted in Figure 29.

### 4.3.3 Collection of Data

The time-axis of the readout (x-y recorder) was calibrated by observing the arrival at the detector of the leading edge of laser pulses reflected from solid targets at distances of R=0, 200 and 400 feet. Having thus established the position of t = o (and of R = 0), the output of the horizontal (R) amplifier of the X-Y recorder was balanced to zero volts and monitored with a digital voltmeter. The position of R = 0 on each data trace was then referred to zero volts, with 0.1% reproducibility. Range accuracy, associated with uncertainty in selecting the initial position of R = 0, was about $\pm$1 meter. The range resolution of the lidar was much coarser, being limited in the present case (for GaAlAs) to about 40 feet by such factors as transient recorder-waveform eductor resolution, PMT transit-time spread and, for non-ideal (i.e., non-uniform) fog conditions, the shape of the laser pulse. The latter dependence stems from the fact that the computer program

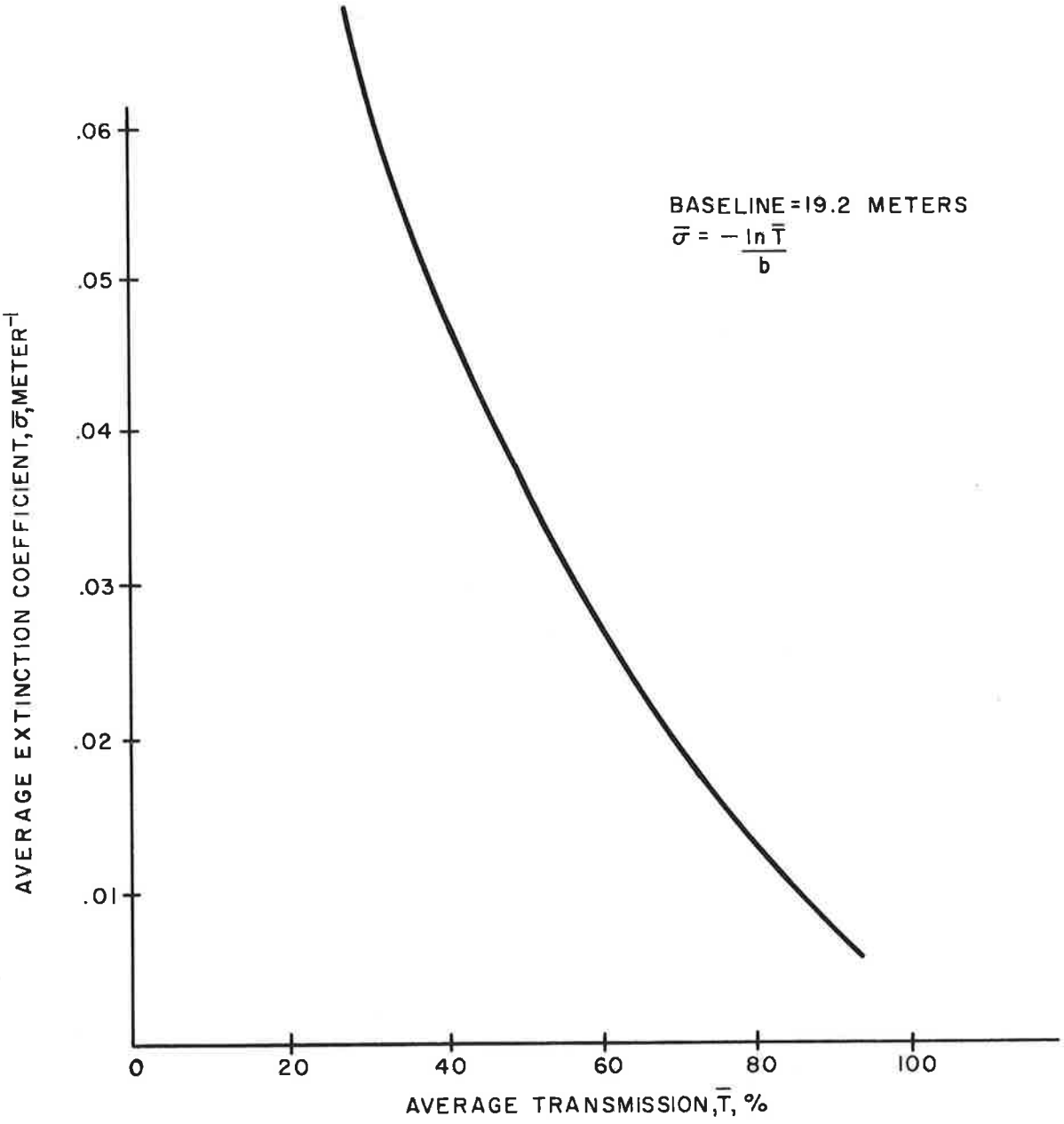


Figure 29. Extinction coefficient $\bar{\sigma}(\bar{T})$, averaged over eight bins, versus transmission T, as measured by 19.2 meter baseline transmissometers

which "subtracts" the laser pulse shape from the lidar returns is based on the assumption of homogeneity. For the ruby system the resolution is expected to be better, perhaps 10-15 feet.

The chamber was then filled with fog and once a persistent value of average transmission $\bar{T}$ was reached, several lidar traces were taken. Usually the traces were "rerun" with the shutter closed, to obtain the zero line. This was a critical step, especially for the GaAlAs data, since the waveform eductor had a baseline which varied significantly (for zero input signal) as one swept the horizontal (time) axis. This spurious output is due to leakage of the one hundred FET's associated with the individual integrating capacitors. Since each FET is slightly different from every other, the output baseline, in the absence of a signal, has essentially 100 different values. This irreducible "noise level" is virtually constant, appearing in the same relationship to the origin of the time axis for each scan. Thus, by tracing the FET noise on the same recording as the signal, the spurious part can be subtracted. Figure 30 shows an example of the data as it appears before and after this zero-correction.

### 4.3.4 Results

4.3.4.1 GaAlAs System - There are several features which stand out in the results of the Richmond field tests. These are now summarized briefly.

Averaging of the GaAlAs lidar returns by the waveform eductor yields relatively smooth traces. The analysis of these traces seems to indicate a lack of homogeneity through the chamber.

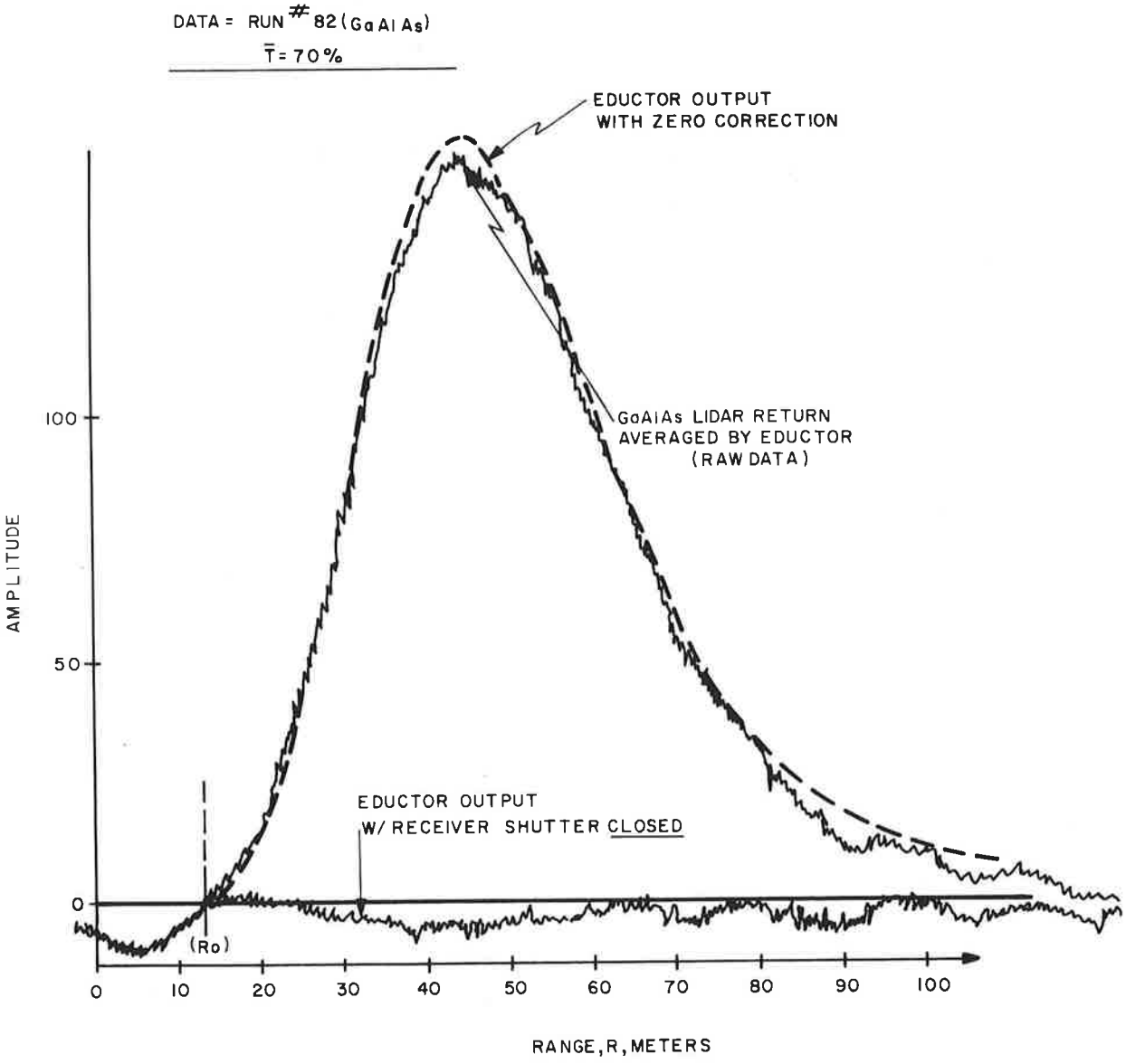


Figure 30. Output of waveform eductor, showing the signal from the lidar and the residual FET noise (see text) with laser light blocked off. The dashed curve is the corrected signal

However, there is no discernable relationship between these apparent inhomogeneities and the "wet-dry" pattern arising from imperfect longitudinal diffusion in the chamber (Figure 28).

Separate GaAlAs traces, each averaged over approximately 1 minute and obtained as much as 15 minutes apart but under the same chamber control setting, show excellent reproducibility, indicating that the time constant is sufficient to give representative results (Figure 31).

The results obtained by applying the ratio method (eq.2-7) to the lidar signals show the importance of including the finite laser pulse width in the analysis. Extinction coefficients derived for $R \lesssim 2c\tau_p$ by the short pulse approximation are usually lower than the "more exact" results (finite pulse treatment), often by as much as several hundred percent.

A fairly typical trace is shown in Figure 32, with the extinction coefficients derived from the ratio method shown on the same plot. The short horizontal bars represent $\sigma_{ij}$ over interval $R_j - R_i$. The values of $\bar{\sigma}$ (ratio) and $\sigma$ ($\bar{T}$) are given. The tendency for $\sigma_{ij}$ to increase, as range increases from 70 to 90 meters, is commonly found in the data and may be related to the general pattern of longitudinal segmentation of the fog in the chamber. Unfortunately, the segmentation was not assessed beyond about 60 meters.

The same tendency (low values for $\sigma$) is observed in the S-function (slope) analyses. When only data from ranges $R \gtrsim 2c\tau_p$ are included, the extinction coefficient $\sigma_s$ resulting from the slope calculation is found to correlate reasonably well with $\sigma(\bar{T})$ derived from the transmission $\bar{T}$.

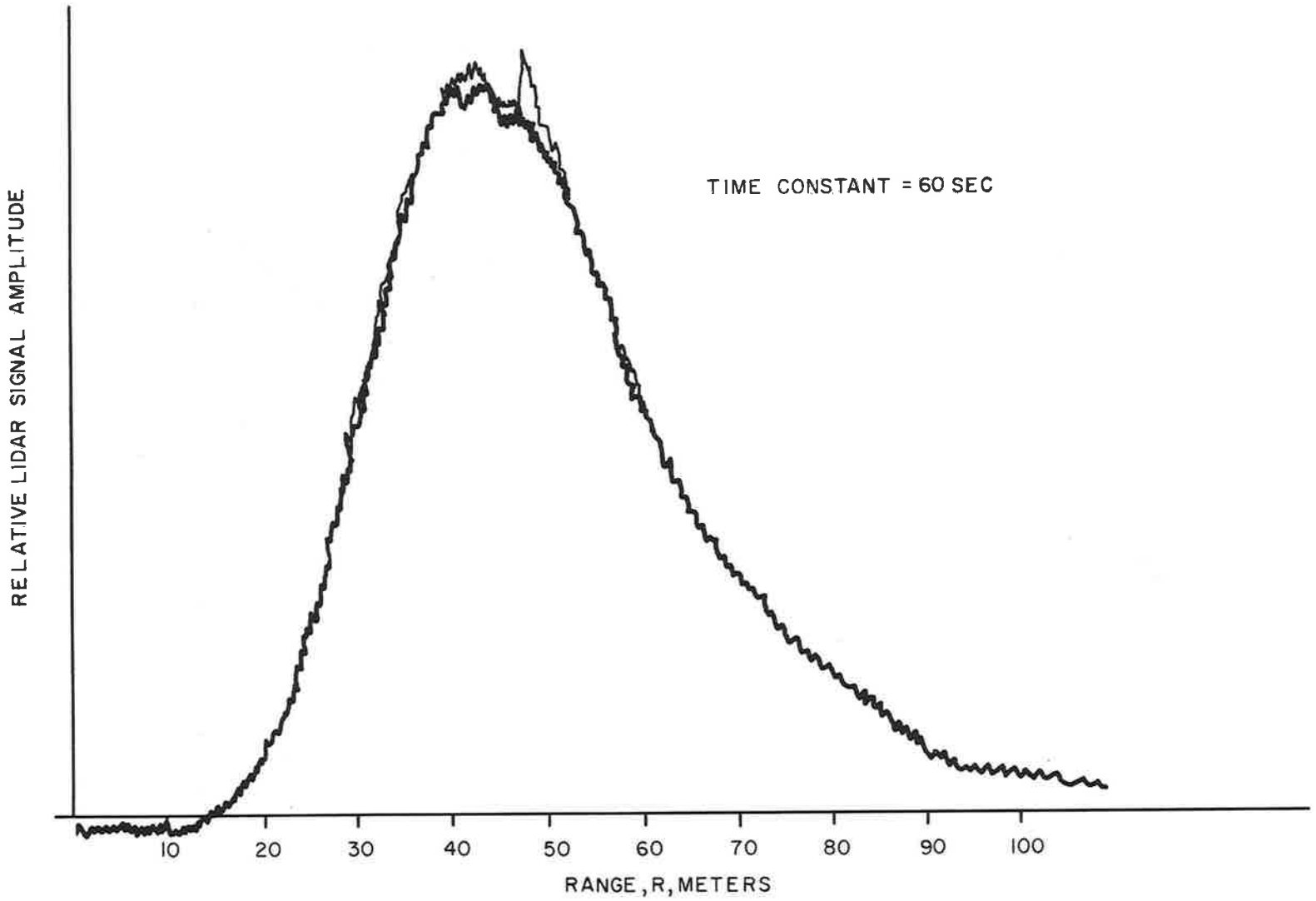


Figure 31. Successive traces (run about 5 minutes apart) of GaAlAs lidar returns, showing characteristic reproducibility (Richmond chamber)

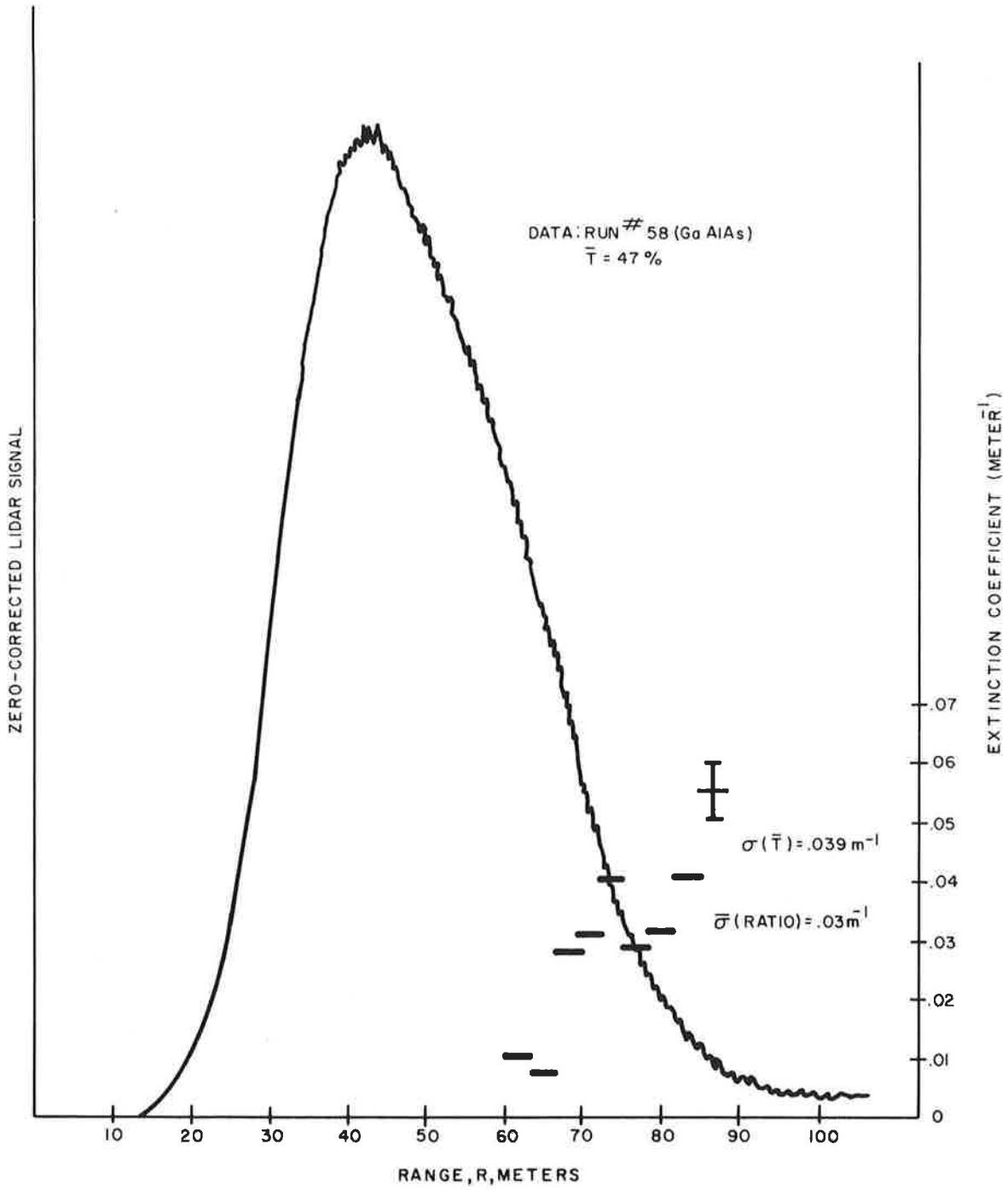


Figure 32. GaAlAs lidar signal (zero-corrected) corresponding to averaged transmissometer reading of $\bar{T}$=47% ($\bar{\sigma}(\bar{T})$ = 0.039m$^{-1}$). Range-resolved $\bar{\sigma}$ (ratio) is also plotted

By filling the distant part of the chamber with fog while leaving the near region empty, well-defined fog banks were produced. Lidar signals obtained with the GaAs system from bank-surfaces at approximately 600, 700 and 800 feet are shown in Figure 33 to simulate a 200 foot ceiling detected at lidar elevation angle of about 15°.

The average extinction coefficients $\bar{\sigma}$ (ratio) determined from twenty-two different lidar runs are plotted in Figure 34 against the transmissometer-derived $\sigma(\bar{T})$ (Sec. 4.3.2) for the same runs. Ideally, the points would fall along a 45° line through the origin. However, the data points have statistical uncertainties, as indicated by the representative error bars in Figure 34 ($\pm$ 1 std dev). In addition, non-random factors, including errors in calibration of transmissometers, chamber inhomogeneity, dissimilar volumes measured by the lidar and the transmissometers, and possible multiple scattering effects, are expected to produce other than ideal results.

To obtain a qualitative idea of the relationship between $\bar{\sigma}$ (lidar) and $\bar{\sigma}$ (transmissometer), the data were fit in two ways.

The first method was simply to force the line through the origin, choosing the slope so that as many runs fall above as below that line. The second method (line 2) is computed from a weighted least squares fit.

The significance of these lines should not be overestimated. The treatment of the data serves only to indicate the qualitative agreement between the two methods (lidar and transmissometer) of measuring extinction.

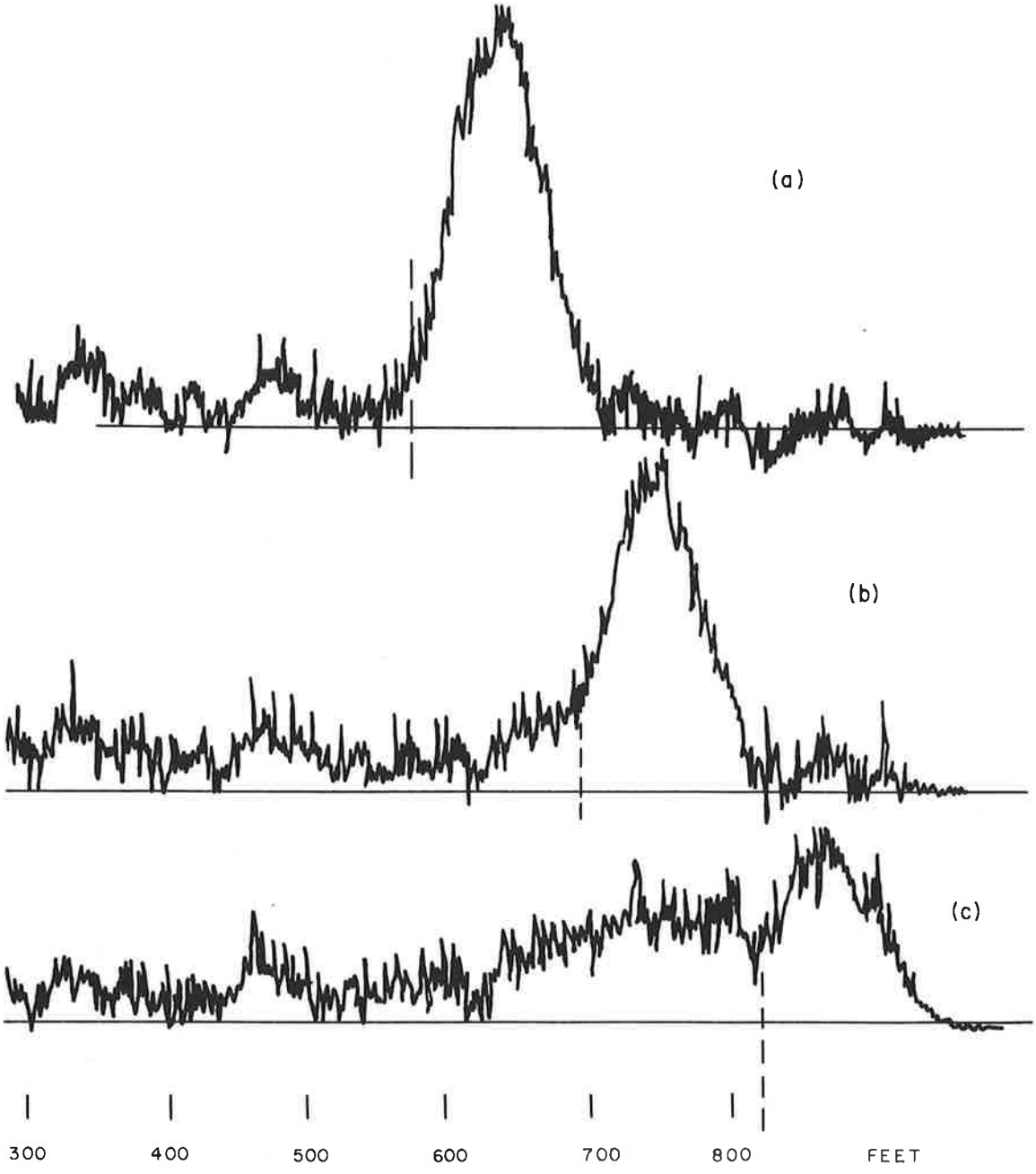


Figure 33. Lidar (GaAlAs) signals from artificial fog banks placed at 600, 700 and 800 feet. Negligible attenuation up to fog bank; extinction coefficient in bank estimated ~ $0.44m^{-1}$

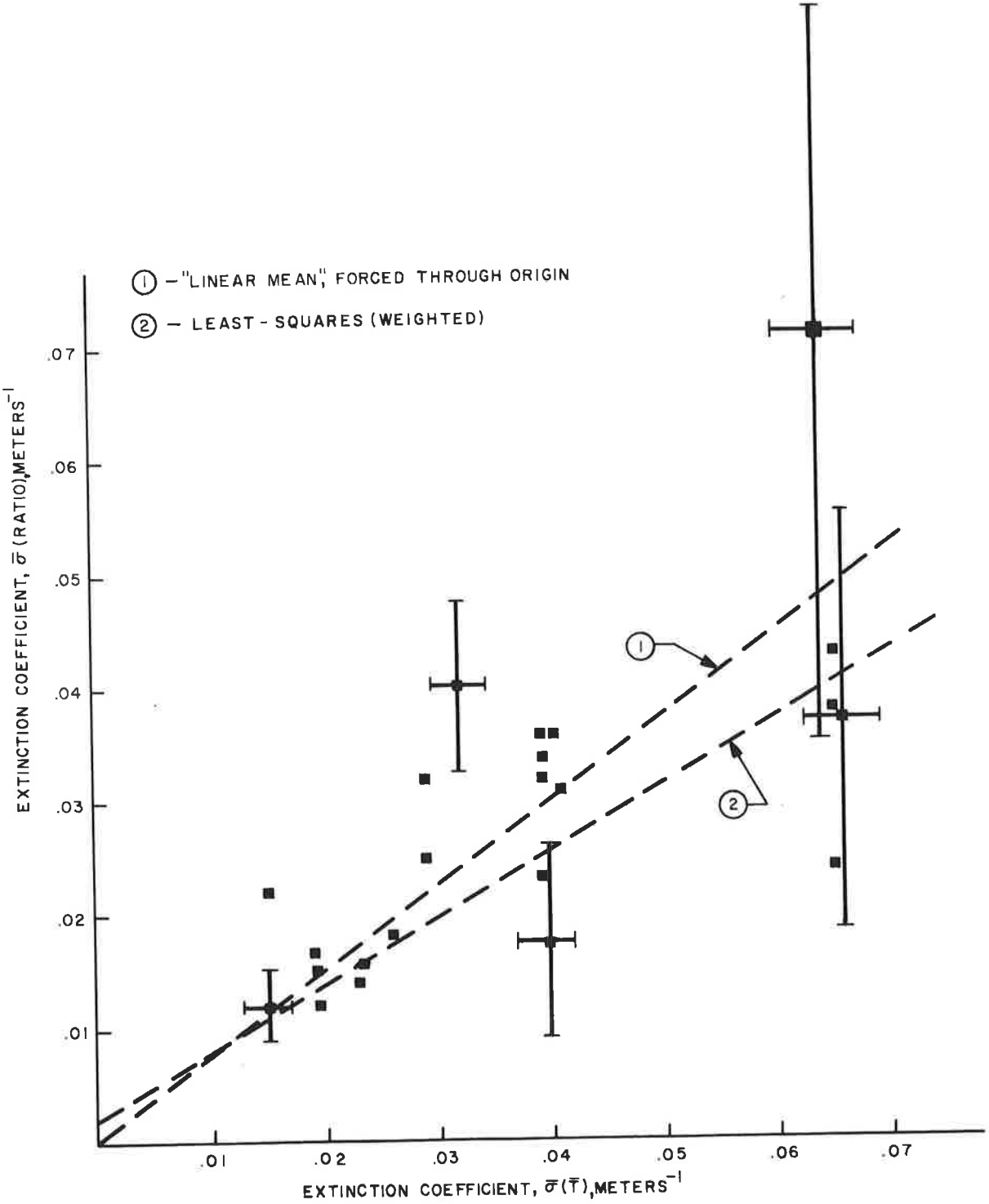


Figure 34. Extinction coefficients measured by lidar (ratio method) vs extinction coefficient determined from average transmissometer reading in chamber. Error bars represent ± 1 standard deviation

4.3.4.2 Ruby System - The most striking results obtained by the ruby lidar were related to the wide variation in signal shapes for successive returns (Figure 35). This is due to the instantaneous structure of the fog as the solenoid-regulated valves go on and off more or less randomly.

The performance of the ruby system was disappointing and a great deal of effort and time was spent overcoming a series of breakdown problems that arose. These problems included contamination of the cooling system to the extent that the entire network of tygon tubing had to be replaced, and the system flushed thoroughly. Also an intermittent malfunction of the charging relay in the power supply caused continual inconvenience and limited the quality of data collected with the ruby lidar.

Other minor difficulties, such as failure of both a flash lamp and the heat-exchanger fan, only served to emphasize the unsuitability of the present design of the ruby laser for field use. In addition to the problems mentioned, the laser threshold and pulse shape was found to vary unpredictably. Since these defects had not been in evidence during pre-test experiments in the laboratory, it seems plausible to attribute them to causes related either to the shipment of apparatus to the fog chamber or to the effects of high humidity on various electronic and/or optical components.

As a result of the foregoing problems, both the quantity and quality of the ruby lidar data were limited. In particular, it proved impossible, due to shot-to-shot variations, to "add" the traces from several successive ruby shots and average the inhomogeneities through the chamber. Furthermore, the variable pulse

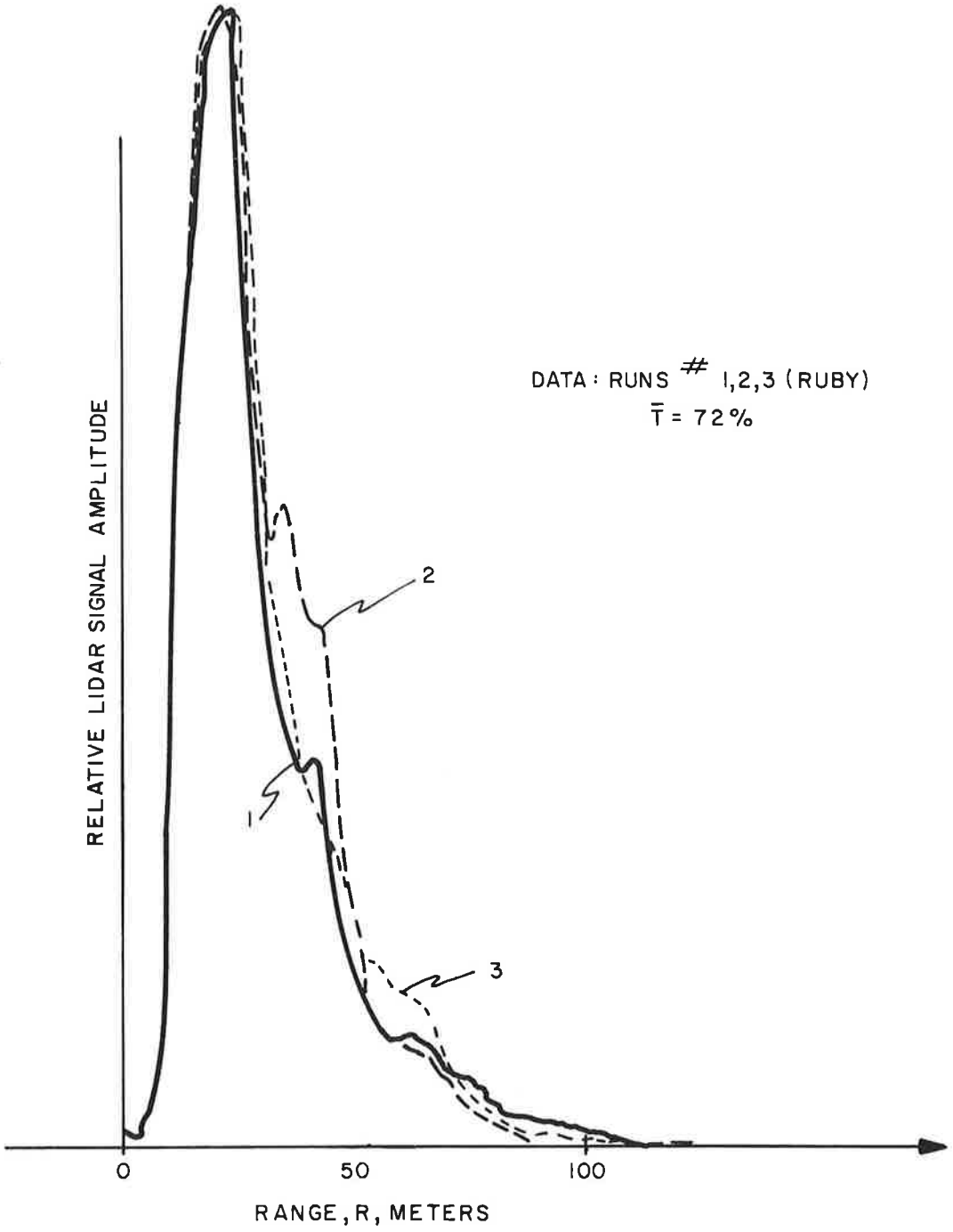


Figure 35. Successive ruby lidar returns, showing characteristic variability of signals under same average fog conditions

shape prevented reliable application of the computer analysis.

Figure 36 shows the results of analyzing two successive ruby lidar returns taken under the same average chamber conditions. In view of the difficulties mentioned above, the results are surprisingly close. This is probably due largely to the relatively long $\Delta R_{AB}$ over which $\sigma_{AB}$ (ratio) is computed.

4.3.4.3 Helium-Neon CW Lidar - Attempts were made to observe a visibility-dependent phase shift in the modulated CW helium-neon radiation reflected from the fog. Theory predicts that, for a given uniform visibility, the relative phase will vary as the modulation frequency is varied, following a tangent curve, with a dramatic change in sign at a characteristic frequency (Figure 2).

With the chamber filled with dense fog (visibility 50-100 feet), the relative phase was monitored as the modulation frequency was varied. While there seemed to be some correlation between relative phase and the frequency, the dependence was weak and over a broad range of frequency, with about 90° total phase shift over a range of 3-4 MHz. Furthermore, no sharp transition occured.

There are at least two possible explanations for this broad dependence. First, the "transition frequency" at such low visibility may be too high for the system. (The gain of the video amplifier for the modulator falls off at 10 MHz; however, at about 8.5 MHz, r.f. pickup begins to cause spurious phase shift readings.)

According to Figure 3, the critical frequency for a visibility ($V_m$) of less than 100 ft. is greater than 7 MHz. In order to lower the critical frequency, the fog density in the chamber was decreased. But it was impossible to increase visibility very

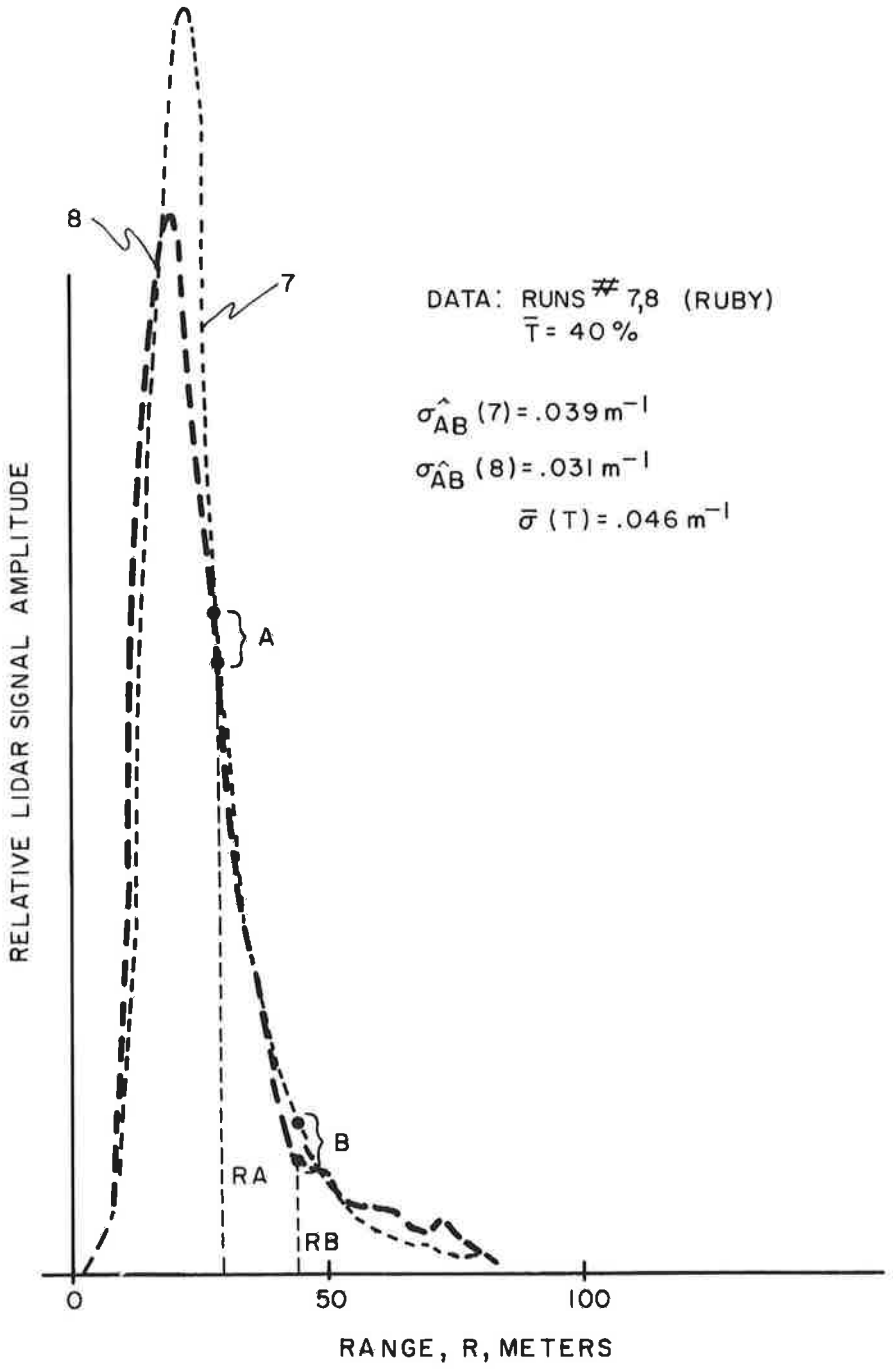


Figure 36. Analysis of ruby lidar traces, obtained from successive laser firings at the same average chamber transmission ($T_{19.2m}$ = 40%)

much (perhaps a factor of 2) before the return lidar signal amplitude was too small to "lock" the phasemeter. In other words, the system lacks sensitivity at visibilities much above the very low values investigated.

The second possible source of a broad frequency dependence is the non-uniformity of the fog. Although this case has not been analyzed theoretically, intuitively it seems that an inhomogenous medium would either cause the sharp frequency dependence to broaden, or it would wipe out the effect entirely.

An attempt was made to reduce inhomogeneity by turning off the air-water inlets and allowing diffusion to homogenize the fog before it decreased in density. No change in the nature of the frequency dependence was observed over short periods; as the fog settled and thinned, the phase (for fixed frequency, 7.5 MHz) fell through about 60° before the signal weakened beyond use.

To summarize the situation regarding the modulated CW lidar:

1. There seems to be evidence for a visibility-dependent relationship between relative phase and modulation frequency.
2. To establish this dependence more certainly, and in particular to demonstrate the expected "sharp" system response, more system sensitivity (i.e., more laser power) is required.

It is felt that the present power would have to be increased by at least 10, and preferably 100 times (i.e., to 30-300 mw). Possible sources would be the CW Argon and Nd: YAG lasers.

3. It is highly questionable whether the additional cost of hardware and man-hours for design, assembly and testing

of a modulated CW system are warranted. Not only is a new laser required, but in all probability the modulator would be altered and a modification would be required in the system layout.

If the effort were to be carried out as a pure research project, it would be easier to justify. However, in the context of developing a prototype for SVR measurement, on the time scale currently being pursued, it seems that the CW scheme is not very attractive. In addition to the still-unproven performance of the device, it appears that serious phase ambiguities might make the method useless in inhomogenous fog conditions. While this limitation might be overcome with the use of a multi-frequency system, the added complexity (and presently unproven status) hardly seems to compare in practicality with a pulsed lidar system.

# 5. CONCLUSIONS

The work described in this report is an investigation of the use of lidar as the basis for low visibility measurements. Several concepts have been tested, both in natural and artificial fogs. Extinction coefficients deduced from lidar signals have been compared with independently-determined values. Reasonable agreement exists between these values with respect to the GaAlAs lidar measurements and, to a more limited extent, to the ruby lidar.

## 5.1 LIMITATIONS OF TSC LIDAR FIELD STUDIES

The results demonstrate the feasibility of determining extinction coefficients and hence visibility with a lidar system. The degree of confidence in the values found in Sec. 4 is not high enough, however, to justify outright statements about the system accuracy. Several factors interfere with the measurements to limit the scope of the conclusions drawn. These are summarized below, almost exclusively with regard to the GaAlAs system.

1) The inhomogeneity of the fog in the chamber has already been detailed. This makes it very difficult, if not impossible, to distinguish real from artificial dispersion in the measured values of $\sigma$ during any given run. If we assume that the chamber inhomogeneity pattern is reproducible, then the fact that not all runs under the "same" fog conditions (as determined by the transmissometer readings) give the same $\sigma$'s indicates that a good part of the variability in the results is due to the

lidar measuring system. (See following comments.) On the other hand, the reproducibility of the fog structure is not assured. It depends in part on the resettability of transmission of each bin (judged to be somewhat crude) and in part on the random pattern of solenoid-firings elicited by the transmissometer readings. It is felt that the latter factors contribute significantly to dispersion in the data.

2) Almost certainly, unknown systematic errors are introduced by the finite width of the laser pulse, which is on the order of the width of the lidar return itself. The computer method for extracting the extinction coefficients, using eq. (2-11), is thought to be correct as far as it goes, but simplifying assumptions such as homogeneity, gaussian pulse shape and the use of a closed-form for f(R) may not sufficiently represent the real situation.

   That the computer treatment may not be adequate is suggested by the fact that when the portion of lidar curves at and near the peak were analyzed, the results were very irregular and often unreasonable. A shorter pulse would help considerably here.

3) A lack of rigor in the means for independently monitoring extinction weakened the significance which might otherwise be attached to the lidar data. The limitations inherent in the chamber transmissometers have already been mentioned. Likewise the problems in using contrast targets have been raised.

4) The base level of the waveform eductor was subject to small spurious drift. It was noticed when making "zero-signal traces" to be used in the FET noise subtraction (4.3.3). Occasionally the zero traces before and after the run were at different DC levels. Though the amplitude of the drift was only a few percent of full scale, this is enough to cause significant error in the resultant lidar amplitude. It is likely that this drift effect is a major source of the large dispersion and variance apparent in some of the runs of Figure 34.

5) Our entire analysis has been based on single-scattering theory. It is probable that multiple scattering contributes to the lidar profiles, especially with the large fields-of-view used in the GaAlAs work. While future work should include a closer study of the effects of higher-order scattering, no attempt was made to treat them here. Considering the pulse-width corrections, the large field-of-view, the known "patchiness" of the fog chamber, and the lack of an independent, accurate method to establish the "true" visibility, the magnitude of the additional scattering contribution cannot be found from the present data.

## 5.2 FUTURE PLANS

### 5.2.1 Improvements in Test Procedures

In light of the above comments, there are several items which demand attention before further tests are pursued in the field.

The following discussion deals with the GaAlAs system.

1) A shorter laser pulse is essential. The power supply and diode array driver circuit for the TSC GaAlAs source is currently being altered to reduce the pulse width to about 35 nsec. The peak power and pulse rate will not be affected.

2) A method must be found for relating lidar-deduced extinction to a reliable independent reference measurement, even in the presence of an inhomogeneous atmosphere. One way to monitor the extinction over a known path is by the use of a series of partially and totally reflecting targets distributed along a direction parallel to and near the actual lidar probe path.[12] The reflectivity of these targets can be calibrated in the absence of atmospheric attenuation and then used, by aiming alternately at the targets and at free space, as references for attenutation in fog.
Of course the method is only as good as the spatial and temporal conditions allow. (In this case, it is necessary that both paths encounter the same average extinction during the sampling period chosen. Unfortunately, the effective "sampling" period may be much longer than any averaging intervals, due to aiming procedures, filter changes, etc.) The difficulty of obtaining such reference comparisons simultaneously and spatially superimposed seems to be common to all methods in use.

3) The one degree beam divergence of the GaAlAs system was dictated by the relatively large diode array. Future work should use sources with smaller fields-of-view to minimize multiple scattering effects, Brown,[4] for example, used fiber-optic coupled GaAs diode arrays to obtain a beam angle of one-third of a degree (6 mrad).

4) Signal processing must be brought to the state where raw signals can be handled automatically (in real time if possible). This will reduce the burden of analysis and expedite feedback to the operator so critical adjustments can be made during the limited time usually available for visibility-type measurements.

   The Biomation transient recorder can serve as the basis for such processing with a direct digital readout coupled via an appropriate interface to a computer or magnetic storage disk.

   A corollary benefit of such a procedure would be the elimination of the troublesome drift associated with the (analog) eductor method.

### 5.2.2 A Look Ahead

Our work, and that of Brown,[4] Viezee et al,[3] and others, indicates that lidar can in fact give quantitatively meaningful measurements of extinction.

There are of course technical aspects which put realistic limits on the effective probing range of the lidar and on its applicability to airport requirements. These aspects include

dynamic range of both the detector and receiver, signal-to-noise limitations, and the need to correct for higher-order scattering effects. Also eye safety criteria must be met.

Finally, any instrumental approach to the measurement of SVR must be judged with regard to operational needs of pilots and air traffic controllers. Factors relating to the lidar, such as sampling range, response time, ready interpretability of instrument output, accuracy and reliability under complex visibility conditions, must be discussed in a manner which integrates the technical and operational requirements of an approach-visibility system.

# APPENDIX

## UTILIZATION INSTRUCTIONS FOR OPERATION OF THE LIDVIS PROGRAM ON THE PDP-10 COMPUTER

by

Wolfram Blättner and Reece Small*

*Radiation Research Associates, Inc., 3350 Hulen Street, Fort Worth TX 76107

## A-1. INTRODUCTION

The LIDVIS program was written in order to assist in analyzing visibility measurements taken in foggy atmospheres with a lidar-back-scatter system. The program is based upon single scattering theory assuming homogeneous atmospheres. The program computes visibility data for a given lidar pulse shape. Visibility data that are obtained from calculations based on the "short-pulse theory" are also printed out for comparison.

The purpose of these instructions is to identify all information required as input to the LIDVIS program, to designate the proper format for all data required in the input data deck, and to provide additional information on the interpretation of the printed output.

standard visibility of 100 meters. $X_o$ [Eq. (A-5)] was taken to 9m. The pulse shapes were assumed to be described 1) by a square-shaped pulse of pulse width $\tau_p$ = 100 ns, 2) by a Gaussian pulse with DT = 25 ns and TX = 45 ns, and 3) by a Gaussian pulse with DT = 90 ns and TX = 84 ns. The pulse height was chosen such that the integral

$$\int_0^{\tau_p} P(\tau)d\tau$$

was the same for all three cases. The signal power obtained from these three cases is shown in Figure A-1a. Figure A-1b shows a similar plot for square-shaped pulses with different pulse length [compared with the signal calculated using Eq. (A-2)]. It can be seen that the signal obtained at the receiver is highly-dependent upon the shape of the outgoing lidar pulse. Erroneous data are, therefore, expected if one uses Eq. (A-3) for calculating the extinction coefficient lidar systems having "sizeable" pulse lengths.

Figure A-2 gives the signal power for different standard visibilities using a Gaussian pulse-shape with DT = 90 ns and TX = 84 ns ($X_o$ = 10m). The graph shows the expected increase of the peak power with decreasing visibility. The position of the peak is slightly-dependent upon the visibility conditions.

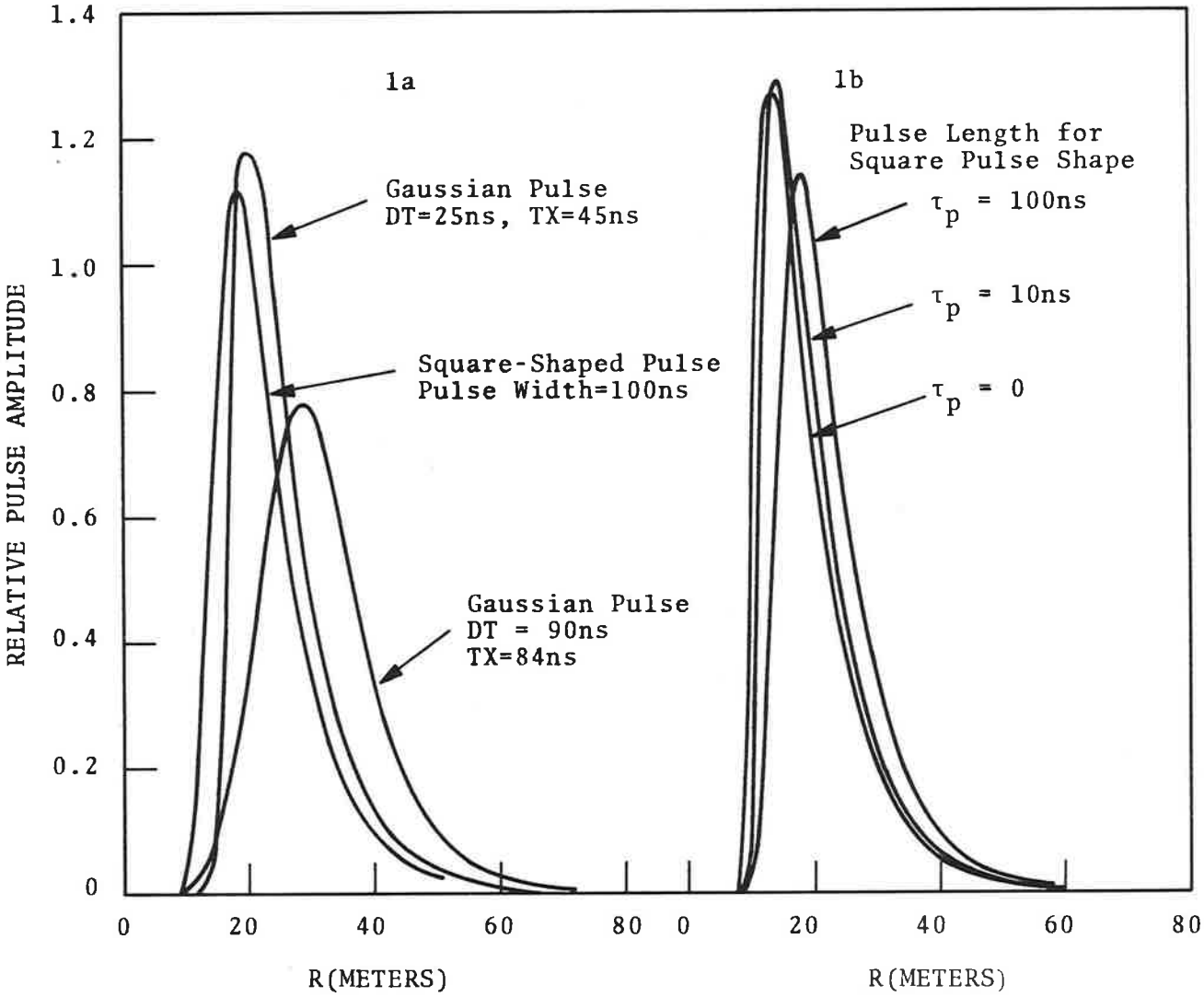


Figure A-1. Receiver pulse vs range for bistatic systems

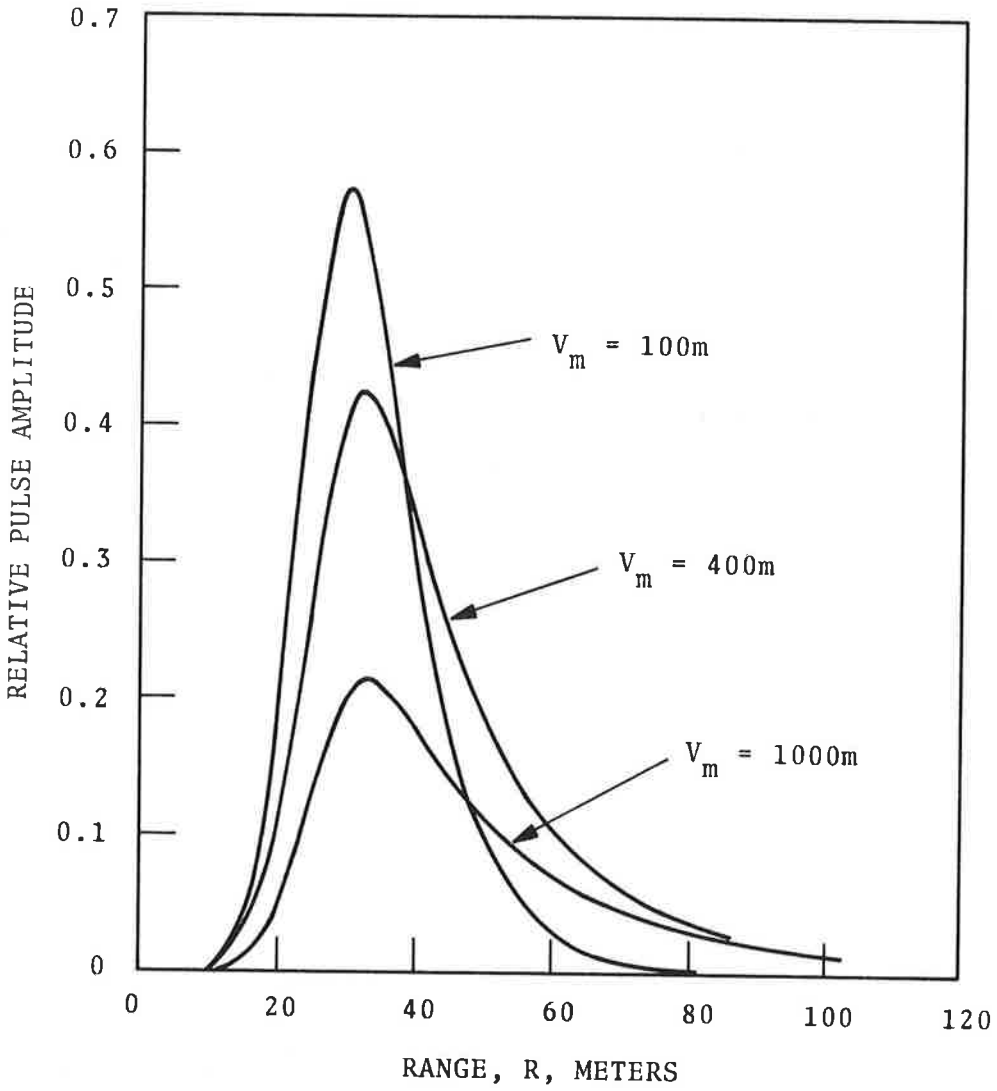


Figure A-2. Signal power for different standard visibilities, $V_m$

## A-3 COMPUTATIONAL DETAILS

The LIDVIS program compares the ratio of the measured signals

$$\rho_p = P(R_i)/P(R_{i+1}) \tag{A-8}$$

with the calculated ratios [see Eq. (A-1)]

$$\rho = \frac{\int_0^{\tau_p} \left[ P_o(\tau)\ f(R_i - c\tau/2)\ e^{-2\sigma R_i} \Big/ (R_i - c\tau/2)^2 \right] d\tau}{\int_0^{\tau_p} \left[ P_o(\tau)\ f(R_{i+1} - c\tau/2)\ e^{-2\sigma R_{i+1}} \Big/ (R_{i+1} - c\tau/2)^2 \right] d\tau} \tag{A-9}$$

The value of $\rho$ is calculated for three different values of $\sigma$ with the starting values taken as $\sigma_{max} = .3912$, $\sigma_{med} = 7.829 \times 10^{-3}$, and $\sigma_{min} = 3.912 \times 10^{-3}$, corresponding to visibilities of 10, 500, and 1,000 meters, respectively. Choosing the interval around $\rho_p$, LIDVIS takes the average of a new $\sigma_{med}$ and reiterates the process. For example, if $\rho(\sigma_{med}) > \rho_p > \rho(\sigma_{min})$,

$$\sigma_{max} = \sigma_{med} = \sigma$$

$$\sigma_{med} = (\sigma_{med} + \sigma_{min})/2.0$$

$$\sigma_{min} = \sigma_{min} \quad .$$

This process is continued until

$$(\sigma_{med} - \sigma) \ / \ \sigma_{med} < 0.01.$$

Error messages ("PULSE RATIO OUT OF RANGE") are printed out should the ratio of the measured pulses lead to visibilities smaller than 10m or larger than 1000m.

above for the generation of the LIDVIS.F4 file. The input data are entered through the remote terminal by giving the command MAKE FORØ5.DAT or MAKE FORØ1.DAT and then typing in the data in the proper format.

The program is ready to run after the source deck has been compiled and the necessary data files have been created. This is done by giving the command EXECUTE LIDVIS. The printed output may be obtained on the PDP-10 printer or the remote terminal by giving the command LIST FORØ6.DAT or TYPE FORØ6.DAT, respectively.

## A-5 INPUT INSTRUCTIONS

The LIDVIS program is designed to run several problems back-to-back, assuming that the same lidar system is used for each one of these problems. The program reads in the title, ranges, and signal data for each problem from either cards (NIPT=5) or tape (NIPT=1).

Geometrical overlap function and pulse shape may be calculated in the program [Eqs. (A-5), (A-6), and (A-7)] or (optional) be read in from cards. In case the overlap function is input from cards, LIDVIS uses a linear interpolation to calculate the values of $f(R-c\tau/2)$.

A description of the input items and the required formats is given in Table A-1.

TABLE A-1. INPUT DATA FOR LIDVIS

| CARD | FORMAT | INPUT ITEM | DEFINITION | LIMIT |
|---|---|---|---|---|
| 1 | 2I10 | NPROB | Number of problems to be included in one run | |
| | | NIPT | Number of input tape to read title, R(I) and P(I) values | |
| 2** | 2A4 | TITLE | Description of Data | |
| 3 | | IFUNC | Geometrical Overlap Function I.D. IFUNC = 1 for Bistatic System [Eq. (A-5)] IFUNC = 2 for Coaxial System [Eq. (A-6)] IFUNC = 3 for Inputting Values for Overlap Function | IFUNC=1,3 |
| | 5I10 | NR | Number of Ranges Input | |
| | | IP | Laser Output Pulse ID IP=1 for "Square" Pulse IP=2 for Gaussian Distribution of Pulse [Eq. (A-7)] IP=3 Pulse Distribution input from Cards | IP=1,3 |
| | | NINT | Number of intervals in integral over pulse length | |
| | | NF3 | Number of input values for overlap functions (omit if IFUNC<3) | |
| 4 | 3E10.3 | TP | Pulse length (nanoseconds) | |
| | | DT | Constant in Eq. (A-7) (Omit if IP≠2) | |
| | | TX | Constant in Eq. (A-7) (Omit if IP≠2) | |
| 5 | 8E10.3 | PO(J) | Values for Lidar Pulse (Omit if IP≠3) | J=1,NINT+1 |
| 6 | E10.3 | TAU(J) | Time values Corresponding to PO(J) Values (nanoseconds) (Omit if IP≠3) | J=1,NINT+1 |

| CARD | FORMAT | INPUT ITEM | DEFINITION | LIMIT |
|---|---|---|---|---|
| 7 | E10.3 | RO | See Eq. (A-5) (Omit if IFUNC≠1) | |
| | | CONS | See Eq. (A-6) (Omit if IFUNC≠2) | |
| 8 | 8E10.3 | FR(I) | Range Values (meters) Corresponding to Input Geometrical Overlap Function Values (Omit if IFUNC≠3) | I=1,NF3 |
| 9 | 8E10.3 | FX(I) | Geometrical Overlap Function Values Corresponding to FR(I) Values (Omit if IFUNC≠3) | I=1, NF3 |
| 10 | F5.0 | R(I)*,** | Ranges (meters) for which pulse height data are to be input | I=1,NR |
| 11 | F5.0 | P(I)** | Pulse height measured at receiver, corresponding to R(I) | I=1,NR |

---

*If desired, Card 10 could be used to input the times (in seconds) at which the pulse-height data [P(I)] are to be input on Card 11. If the input values of R(I) are times, then additional cards must be input to the source deck for LIDVIS which convert the input time values to ranges in meters.

**Cards 2, 10, and 11 have to be read in from tape NIPT for each NPROB problem. All of the other cards have to be read in only for the first problem.

## A-6 PROGRAM OUTPUT

Table II gives the input data for a sample problem. The program was run for only one problem. The visibility is calculated for 10 ranges, the values of the receiver signal and of the distances are read in from cards. Equation (A-5) was used to describe the overlap function assuming a value of $X_o$ = 10 meters. The pulse shape is given by Eq. (A-7) with TX and DT taken to be 90 and 84, respectively. One-hundred intervals are used to integrate over the pulse length of 180 ns.

The first table printed out by the LIDVIS program gives a description of the system being used (overlap function, pulse description: Table III). The following tables will then print the visibility as a function of range for both the short-pulse assumption and for the lidar pulse input (Table IV). The visibilities are then averaged over all ranges. For the visibilities calculated from the short-pulse assumption, the average visibility is obtained only from those ranges that lead to positive values of the visibility.

## A-7. PROGRAM LISTING

```
      COMMON   RO,PI,X,IFUNC,CONS,FR(100),FX(100),NF3
      DIMENSION R(50),P(50),SIGMA(4),VIS(2),RATIO(2,4),TITLE(2)
     1,TAW(101),PO(101),AVE(3)
C
    1 FORMAT(1H1, 1X,'RADIATION RESEARCH ASSOCIATES   FORT WORTH, TEXAS
     1  PROGRAM LIDVIS'//)
    5 FORMAT( 2A4)
    6 FORMAT(// 2X, 2A4)
   11 FORMAT(8I10)
   12 FORMAT(/ 2X,'LIDAR OUTPUT PULSE ')
   14 FORMAT( 7X,'(',I1,')    PO(TAU) = CONSTANT')
   16 FORMAT( 7X,'(',I1,')    PO(TAU) = CONSTANT*EXP(-LN(16)*(TAU-',F4.0,
     1')**2/',F4.0,'**2)')
   17 FORMAT( 7X,'(',I1,')    PO(TAU) = INPUT DATA'/13X,'TAU VALUES =')
   18 FORMAT( 2X, 8F8.2)
   19 FORMAT(13X,'CORRESPONDING PO VALUES =')
   20 FORMAT(13X,'PULSE LENGTH =',F6.1,' NANOSECONDS'/, 2X,'GEOMETRICAL
     1OVERLAP FUNCTION ')
   22 FORMAT(8E10.3)
   23 FORMAT(F5.0)
   26 FORMAT( 7X,'(',I1,')    F(R) = 0.0 IF R IS LESS THAN RO (',F8.5,')'
     1/13X,'F(R) = 2*( ACOS(RO/R)-(RO/R)*SQRT(1-(RO/R)**2))/PI')
   31 FORMAT( 7X,'(',I1,')    F(R) = TANH(',F8.2,'*R)**3')
   36 FORMAT( 7X,'(',I1,')    F(R) = INPUT DATA'/13X,'R VALUES =')
   37 FORMAT(13X,'CORRESPONDING F VALUES =')
   39 FORMAT(///21X,'VISIBILITY AS A FUNCTION OF RANGE'// 5X,'RANGE',6X,
     1'EXTINCTION COEFFICIENT',3X,'VISIBILITY',3X,'VISIBILITY FROM'/ 3X,
     2'(METERS)',11X,'(1/METERS)',10X,'(METERS)',5X,'''SHORT PULSE'''/
     357X,'ASSUMPTION'/)
  359 FORMAT(    F6.1,' -',F5.1,1X,'PULSE RATIO OUT OF RANGE     LT 10.
     1 ',7X,F7.0)
  451 FORMAT( 2X,1P4E10.3)
  361 FORMAT(    F6.1,' -',F5.1,1X,'PULSE RATIO OUT OF RANGE   GT10000.
     1 ',7X,F7.0)
  501 FORMAT(    F6.1,' -',F5.1, 8X,F10.5,2X,2( 9X,F7.0))
  502 FORMAT(    F6.1,' -',F5.1,45X,F7.0)
  999 FORMAT(///)
C
      AL16  = 4.*ALOG(2.)
      PI       =ATAN(1.)*4.
      C        =2.997525E8
      READ(5,11)NPROB,NIPT
      WRITE(6,1)
C
C
      DO 1001 KASE = 1, NPROB
      READ(NIPT,5)   TITLE
      IF(KASE.GT.1)           GO TO 38
      READ(5,11)   IFUNC,NR,IP,NINT,NF3
      READ(5,22)   TP,DT,TX
      VAL      =FLOAT(NINT)
      NINT     =NINT+1
      WRITE(6,12)
      IF(IP.EQ.1)   WRITE(6,14)   IP
```

```
      IF(IP.EQ.2)    WRITE(6,16)IP,TX,DT
      IF(IP.LT.3)    GO TO 21
      READ(5,22)    (PO(J),J=1,NINT)
      READ(5,22)   (TAW(J),J=1,NINT)
      WRITE(6,17)    IP
      WRITE(6,18)    (TAW(J),J=1,NINT)
      WRITE(6,19)
      WRITE(6,18)    (PO(J),J=1,NINT)
   21 WRITE(6,20)TP
      GO TO (25,30,35),IFUNC
   25 READ(5,22)    RO
      WRITE(6,26)IFUNC,RO
      GO TO 38
   30 READ(5,22)    CONS
      WRITE(6,31)    IFUNC,CONS
      GO TO 38
   35 READ(5,22)    (FR(I),I=1,NF3)
      READ(5,22)    (FX(I),I=1,NF3)
      WRITE(6,36)    IFUNC
      WRITE(6,18)    (FR(I),I=1,NF3)
      WRITE(6,37)
      WRITE(6,18)    (FX(I),I=1,NF3)
C
   38 READ(NIPT,23)    (R(I),I=1,NR)
      READ(NIPT,23)    (P(I),I=1,NP)
      AVE(1) =0.
      AVE(2) =0.
      AVE(3) =0.
      NAUR   = 0
      NAUR2  = 0
      DISTM2= R(1)
      DISTM1= R(1)
      WRITE(6,1)
      WRITE(6,6)    TITLE
      WRITE(6,39)
      POT=1.
      TP=TP/VAL
      NR        =NR-1
C
      DO 900 I = 1, NR
      IF(IFUNC.EQ.3)    GO TO 60
      X         =R(I)
      CALL PULSE(F1)
      X         =R(I+1)
      CALL PULSE(F2)
   60 IF(P(I).GT.1.E-10)      GO TO 80
   61 VIS(1)= 0.
      GO TO 360
   80 IF(F1.LE.0.0)    GO TO 61
  140 SIGMA(1)=0.5*ALOG((R(I)/R(I+1))**2*P(I)*F2/(P(I+1)*F1))
     1  /(R(I+1)-R(I))
      VIS(1)   =3.912/SIGMA(1)
      RATIO(1,1)=P(I) /P(I+1)
      IF(VIS(1).LE.0.0)    GO TO 150
```

```
      AVE(3) =AVE(3)+VIS(1)
      IF (NAUR2.EQ.0)          DISTM2 = R(I)
      NAUR2 = NAUR2+1
  150 SIGMA(2)=3.912/10000.
      SIGMA(3)=3.912/500.
      SIGMA(4)=3.912/10.
      I1       =I
      I2       =I+1
      ICHK   =1
      ID       =2
  250 DO 275 IR=1,2
      DO 275 ISIG=ID,4
  275 RATIO(IR,ISIG)=0.
C
      DO 300 INC = 1,NINT
      VAL      =FLOAT(INC-1)
      TAU      =TP*VAL
      GO TO (290,281,283),IP
  281 POT    =EXP(-AL16*((TAU-TX)/DT)**2)
      GO TO 290
  283 POT      =PO(INC)
      TAU      =TAW(INC)
C
  290 DO 300 IR=I1,I2
      X        =R(IR)-C*TAU*1.0E-9/2.
      IF(X.LT.1.)              GO TO 300
      CALL PULSE(FUN)
      IF(FUN.EQ.0.)            GO TO 300
      II     =IR-I+1
      CONST =POT*C*FUN*TP/X**2
      DO 299 ISIG=ID,4
      RATIO(II,ISIG)=RATIO(II,ISIG)+CONST*EXP(-2.*SIGMA(ISIG)*X)
  299 CONTINUE
  300 CONTINUE
C
      DO 350 ISIG = ID,4
      IF(RATIO(2,ISIG).EQ.0.)GO TO 345
      RATIO(1,ISIG)=RATIO(1,ISIG)/RATIO(2,ISIG)
      GO TO 350
  345 RATIO(1,ISIG)=1.E30
  350 CONTINUE
      CHECK    =ABS((SIGMA(4)-SIGMA(3))/SIGMA(4)       )
  351 IF(CHECK.LT.0.01)    GO TO 500
      IF(ICHK.GT.1)            GO TO 390
      ICHK   =2
      IF(RATIO(1,1).LT.RATIO(1,2)) GO TO 360
      IF(RATIO(1,1).LE.RATIO(1,4)) GO TO 390
      WRITE(6,359)    R(I),R(I+1),VIS(1)
      WRITE (6,451) (RATIO(1,KK),KK=1,4)
      GO TO 900
  360 WRITE(6,361)  R(I),R(I+1),VIS(1)
      GO TO 900
  390 IF(RATIO(1,1).GT.RATIO(1,3))    GO TO 400
      SIGMA(4)=SIGMA(3)
```

```
      SIGMA(3)=(SIGMA(3)+SIGMA(2))/2.
      GO TO 250
  400 SIGMA(2)=SIGMA(3)
      SIGMA(3)=(SIGMA(4)+SIGMA(3))/2.
      GO TO 250
  500 VIS(2)  =3.912/SIGMA(4)
      WRITE(6,501)   R(I),R(I+1),SIGMA(4),VIS(2),VIS(1)
      AVE(1) =AVE(1)+SIGMA(4)
      AVE(2)=AVE(2)+VIS(2)
      IF (NAUR.EQ.0)          DISTM1 = R(I)
      NAUR  = NAUR+1
  900 CONTINUE
C
C
      WRITE(6,999)
      IF (NAUR .EQ.0)         NAUR  = 1
      IF (NAUR2.EQ.0)         NAUR2 = 1
      AVE(1) =AVE(1)/NAUR
      AVE(2) =AVE(2)/NAUR
      AVE(3) =AVE(3)/NAUR2
      WRITE(6,501) DISTM1,R(NR+1),AVE(1),AVE(2)
      WRITE(6,502) DISTM2,R(NR+1),AVE(3)
 1001 CONTINUE
C
C
      STOP
      END



      SUBROUTINE PULSE(FUN)
C
      COMMON   RO,PI,X,IFUNC,CONS,FR(100),FX(100),NF3
C
      GO TO(30,50,60),IFUNC
   30 IF(X.GT.RO)   GO TO 40
      FUN      =0.
      RETURN
   40 FUN      =RO/X
      FUN      =2.*( ACOS(FUN)-FUN*SQRT(1.-FUN**2))/PI
      RETURN
   50 FUN      =TANH(CONS*X)**3
      RETURN
   60 DO 70 I=2,NF3
      IF(X.LT.FR(I))          GO TO 80
   70 CONTINUE
   80 FUN   =FX(I-1)+(X-FR(I-1))*(FX(I)-FX(I-1))/(FR(I)-FR(I-1))
C
      RETURN
      END
```

## REFERENCES


1. Brown, R. T., Backscatter Signature Studies for Horizontal and Slant Range Visibility, Final Report No. FAA-RD-67-24, available from DDC: AD-659-469 (1967).
2. Collis, R. T. H., "Lidar," Appl. Opt. 9, 1782 (1970).
3. Viezee, W., J. Oblanas and R. T. H. Collis, Slant Range Visibility Measurement for Aircraft Landing Operations. Final Report AFCRL No. 72-0154 (1972).
4. Brown, R. T., "A New Lidar for Meteorological Application", J. Appl. Meteor. 12, 698 (1973).
5. Moroz, E. Y., J. P. Segre and N. R. Truscott, "Design and Testing of an Erbium Laser Rangefinder for Use as a Ceilometer." Fifth Conference on Laser Radar Studies of the Atmosphere, Williamsburg, VA, June 4-6, 1973.
6. Schappert, G. T., "Technique for Measuring Visibility", Appl. Opt. 10, 2325 (1971).
7. See, e.g., G. T. Schappert, "Visibility Concepts and Measurement Techniques for Aviation Purposes", Final Report DOT-TSC-FAA-71-25, July, 1971.
8. Fenn, R. W., "Correlation Between Atmospheric Backscattering and Meteorological Visual Range", Appl. Opt. 5, 293 (1966).
9. Twomey, S. and H. B. Howell, "The Relative Merit of White and Monochromatic Light for the Determination of Visibility by Backscattering Measurements", Appl. Opt. 4, 501 (1965).
10. Middleton, W. E. K., "Vision Through the Atmosphere", (University of Toronto Press, Toronto, 1952).

11. Horning, D. O. and D. M. Finch, "Historical Summary of Activities in the UC-FAA Fog Chamber Under Contract ARDS-434", Report No. FAA-RD-71-94, August, 1971.

12. Collis, R. T. H., W. Viezee, E. E. Uthe and J. Oblanas, "Visibility Measurement for Aircraft Landing Operations", Final Report, Contract No. F19628-70-C-0083, Air Force Cambridge Research Labs (September, 1970).